22

23

24

25

26

Extensive young silicic volcanism produces large deep submarine lava flows in 1 2 the NE Lau Basin 3 Robert W. Embley* (NOAA/PMEL, Newport, OR 97365 USA) 4 robert.w.emblev@noaa.gov 5 6 Kenneth H. Rubin (Dept. of Geology and Geophysics, U. of Hawaii 7 Honolulu, HI 96822 USA) 8 krubin@hawaii.edu 9 10 *Corresponding author 11 12 Keywords: Lau Basin, dacite, lava flows, submarine 13 **Abstract** 14 New field observations reveal that extensive (up to ~402 km²) aphyric, glassy dacite lavas were 15 erupted at multiple sites in the recent past in the NE Lau basin. This discovery of volumetrically 16 17 significant and widespread submarine dacite lava flows extends the domain for siliceous effusive 18 volcanism into the deep sea. Although several lava flow fields were discovered on the flank of a 19 large silicic seamount, Niuatahi, two of the largest lava fields and several smaller ones ("northern 20 lava flow fields") were found well north of the seamount. The most distal portion of the

northernmost of these fields is 60 km north of the center of Niuatahi caldera. We estimate that

more than 10 km. Camera tows on the shallower, near-vent areas show complex lava

lava flow lengths from probable eruptive vents to the distal ends of flows range from a few km to

morphology that includes anastomosing tube-like pillow flows and ropey surfaces, endogenous

domes and/or ridges, some with "crease-like" extrusion ridges, and inflated lobes with extrusion

structures. A 2 x 1.5 km, 30-m deep depression could be an eruption center for one of the lava

flow fields. The Lau lava flow fields appear to have erupted at high effusion rates and possibly reduced viscosity induced by high magmatic water content and/or a high eruption temperature, consistent with both erupted composition and glassy low crystallinity groundmass textures. The large areal extent (166 km²) and relatively small range of compositional variation within the northern lava flow fields imply the existence of large, eruptible batches of differentiated melt in the upper mantle or lower crust of the NE Lau basin. At this site the volcanism could be controlled by deep crustal fractures caused by the long term extension in this rear-arc region. Submarine dacite flows exhibiting similar morphology have been described in ancient sequences from the Archaean through the Miocene and in small batches on seafloor spreading centers.

1.0. Introduction and background

1.1 Geological and tectonic setting

The Tonga intra-oceanic subduction zone (TIOSZ) has the highest subduction and backarc spreading rates on the planet (Zellmer and Taylor 2001). The Lau basin, the backarc region of the TIOSZ, following an initial rifting phase, has been opening along multiple back-arc spreading centers since about ~ 4 Ma (Zellmer and Taylor 2001; Taylor and Martinez 2003) (Fig. 1). The NE Lau basin is defined here as northern section of the backarc region of the Tonga plate (Zellmer and Taylor 2001; Bird 2003) that is bounded on the west, respectively from north to south, by the Northeast Lau Spreading Center, (NELSC) the Mangatolu Triple Junction Spreading Center, and the Fonualei Rift Spreading Center (Fig. 1). The northern boundary of the Tonga Plate is a complex zone marked by the transition from subduction to strike-slip faulting along the Vitiaz lineament marked topographically by the change in strike of the trench from N-S to a more E-W trend (Pelletier et al. 1998; Zellmer and Taylor 2001). An active crustal tear or "STEP" fault (Subduction-Transform-Edge-Propagator (Govers and Wortel 2005) caused by

51

52

53

54

55

56

57

58

59

60

61

62

63

64

65

66

67

68

69

70

71

72

rollback of the trench, has created a zone of oblique shear that has left a trail of spreading centers and rift basins along this northern boundary (Isacks et al. 1969; Millen and Hamburger 1998; Govers and Wortel 2005). The Tofua Arc defines the eastern boundary of the NE Lau Basin. The NE Lau basin has the highest upper mantle temperatures (Wiens et al. 2006), has one of Earth's coolest slab thermal parameters (the product of convergence speed and age), and has among the highest slab water fluxes (van Keken et al. 2011) of any intra-oceanic subduction zone. All these factors probably contribute to the region's tectonic and magmatic complexity, including an unusually large number of active volcanic systems in a relatively small area. Unusual lavas such as boninite occur in the extreme north of the region (Falloon et al. 2007; Resing et al. 2011; Rubin and Embley 2012) and at least two historic eruptions have been documented within the NE Lau Basin (Fig. 1): (1) a short-lived 2008 eruption on the NELSC (Baker et al. 2011), and (2) a years-long Strombolian activity on West Mata, a boninite volcano whose historic eruptive episodes have been documented for the 1996-2011 interval (Clague et al. 2011; Resing et al. 2011; Baumberger et al. 2014; Embley et al. 2014). We have concluded that the NE Lau basin is a "magmatically greedy" back arc, perhaps by capture of some of the magmatic flux from the magmatically anemic neighboring northernmost Tofua Arc (Embley et al. 2009a; Rubin et al. 2013; Lupton et al. 2015). During the 2008 expedition when the two aforementioned ongoing eruptions were discovered, we also mapped extensive areas of seafloor with high acoustic backscatter, most of which we interpret as lava flow fields within the nearby NE Lau "rear arc". We define "rear arc" as the region between the magmatic arc front (Tofua Arc on Fig. 1) and the NELSC (Figs. 1-4). The high backscatter areas include both those on the flanks of Niuatahi seamount (previously known as Volcano "O") and those lying within a 30 km-wide corridor extending northward ~60

km from Niuatahi toward the trench (Figs.1 and 2) (Embley et al. 2009b). Some of the lava flows extend into the southern edge of the Mata rift basin, wherein lie most of the Mata volcanoes (Figs. 2-4), all of which are composed primarily of boninite lava. Nine seafloor dredges and three camera tows were conducted over the high backscatter areas between 2009 and 2011 to determine their morphology, sediment cover, and composition. As reported herein, we establish that they are all dacite lavas, some with unusual morphologies. This was an unexpected result, because extensive submarine dacite flows are rare in modern environments and previously unknown from the deep sea.

Other non-dacite recent lavas contiguous to this northernmost Lau region have a wide range of compositions. The chain of the Mata boninite volcanoes lie to the northeast (Resing et al. 2011; Rubin and Embley 2012; Embley et al. 2014;) and back arc basin basalt (BABB) to basaltic andesite occurs on the NELSC (Fig. 4), including the youngest lavas of NELSC neovolcanic zone (Michael et al. 2009; Clague et al. 2010), with basaltic andesite (Falloon et al. 2007) recovered only about 5 km west of the LL-D lava field (Fig. 4). A small lava knoll ("BoCo" on Fig. 4) has erupted boninite (Rubin et al. 2013). This close geographic continuity of such a range of lava chemistries is intriguing.

1.2 Submarine lava flows

Much is known about the chemical and physical volcanology of effusive submarine basalts produced in a range of eruptive conditions, mostly from studies of mid-ocean ridge basalt (MORB) and analogue modeling. Those that can be chemically mapped as single lava flows are distributed in pillow mounds, lower relief sheet and lobate flows, and dome-like flows along the mid-ocean ridge spreading centers from either point sources or along eruptive fissures (Ballard et al. 1979; Appelgate and Embley 1992; Smith and Cann 1993; Embley and Chadwick 1994;

Fornari et al. 1998; Perfit and Chadwick 1998; White et al. 2000; Sinton et al. 2002; Rubin and Embley 2012; Chadwick et al. 2013; Clague et al. 2013; Deschamps et al. 2014). Larger off-axis mid-ocean ridge basalt eruptions have also been documented in a few studies (Geshi et al. 2007). There have been fewer such studies of back-arc basin basalt (BABB) erupted from back-arc spreading centers (Saunders and Tarney 1979).

Limited quantities of differentiated lavas have been recovered from some mid-ocean ridge and fracture zone environments (Stakes et al. 2006; Wanless et al. 2010; Schmitt et al. 2011; Colman et al. 2012) but, to date, they appear to represent a volumetrically minor portion of lavas sampled along seafloor spreading centers and are usually associated with rift tips, segment ends, graben bounding faults, or other low magma supply regions (Sinton 1983). Petrologically-differentiated magmatic products are somewhat more common on back-arc spreading centers (Lonsdale and Hawkins 1985; Binns and Scott 1993; Taylor et al. 1994; Gribble et al. 1998) and along magmatic arcs, where they are found commonly as lavas, explosive products (from pyroclastic and hydroclastic processes), and endogenous domes (Wright and Gamble 1999; Fiske et al. 2001; Wright et al. 2006; Graham et al. 2008; Stern et al. 2008; Stern et al. 2014).

Despite this body of knowledge, very little is known about the overall distribution of high silica lavas in the ocean basins, their eruptive processes, and their importance in constructing the extrusive ocean crust. In this paper we document the distribution, composition, size and morphology of unusually extensive dacite lava flow fields in a large region where they are the dominant eruptive product, and hypothesize about their eruption conditions, origin, and significance. To our knowledge, this is the first detailed investigation of extensive submarine silicic lava flows in the modern ocean.

2.0. Methods

2.1 Multibeam sonar mapping

The data used here were collected using the R/V *T. G. Thompson* (cruise TN227, November 2008) with a Simrad EM302 multibeam system and the R/V *Kilo Moana* (cruise KM1008, May 2010; KM1024, December 2010; KM1129a, November 2011) with a Kongsberg-Simrad EM122 multibeam sonar mapping system. The data were processed and gridded using [©]MB System and [©]GMT. The 3D images were created using the [©]Fledermaus and ArcMap[©] was used to layer data and to calculate areas of the lava flows. Multibeam data files are available by cuise name (above) through the (NOAA) National Geophysical Data Center.

2.2 Camera tows

The WHOI TowCam system, developed by D. Fornari and others at Woods Hole Oceanographic Institution, was used in this study to visualize the high backscatter lava flow and verify that it was composed of relatively young (lightly sedimented) lava flows. The camera was towed using a 0.322" coaxial cable off the stern of the R/V *Kilo Moana* on cruise KM1008 (28-April to 10-May 2010). In 2010 the camera system used a three megapixel digital still camera, altimeter, a forward looking (obstacle avoidance) sonar, and a Seabird CTD model SBE25 with standard sensors plus a transmissometer to measure water turbidity. Total depth was calculated by adding the depth from the CTD sensor to the altimeter reading at 1 sec intervals. The altimeter and CTD data were available in real time to monitor altitude, bottom temperature and light transmission. The camera system was towed at about 0.25 knots (~0.5 km/hr) to obtain overlapping imagery from the still camera, which was fired at a 10 second interval in synchroneity with a strobe. Details about the operational and instrumentation capabilities of the WHOI TowCam are available at: http://www.whoi.edu/page.do?pid=17619

Final navigation files for the camera data were created by a combination of layback calculation (using the CTD depth and wire out) and adjusting the track to minimize calculated offsets of the along-track multibeam depth profile and the depth profile made with the camera pressure and altimeter data. Approximate location errors for the camera tow data presented in this paper are ≤50 m. Photographic image names were keyed to time of acquisition (which allowed correlation to other logged parameters such as the sensor data), and auto-processed in [®]Adobe Photoshop Elements to obtain maximum contrast and clarity. The mosaics presented in this paper were constructed by cross-matching photos and overlaying them in [®]Adobe Photoshop Elements.

2.3 Rock dredging and lava chemistry

Dredge samples were collected from the high backscatter lava flow regions during the KM1024 expedition (December, 2010) and from primary structures associated with the Niuatahi caldera walls, caldera floor, and extra-caldera flows (LL-A1 and LL-A3) on KM1129a expedition (November-December 2011) (Fig. 4; ESM_1). A standard box-mouth chain bag dredge with 10 kg bottom weight was used, along with a wireline-mounted pinger for bottom location. In order to minimize the spatial sampling scale the dredge distance on bottom was usually limited to 0.5-0.7 km, occasionally up to 1.0 km on low relief surfaces. Start and stop locations and seafloor depth of the ship when the dredge hit and left the sea bed are reported in ESM_1, along with persistent sample identifiers (IGSN, registered at www.geosamples.org) and site locations. Dredge rock recoveries were excellent for most deployments (50-150 Kg) and thus representative of the terrains sampled, although two dredges taken on KM1024 recovered much less. The dredge and all work surfaces were thoroughly cleaned after each deployment to limit cross sample contamination. After recovery samples were dried, sorted and placed into visually

distinct groups based on physical, mineralogical, and alteration characteristics, from which 5 to 10 representatives were given specific sample numbers, described, and subsampled on board for shore-based analysis. Several additional samples were recovered when a camera sled touched the seafloor on KM1008 (May 2010). Two of those samples (from "Motutahi", the young resurgent volcanic cone within Niuatahi caldera) are included here. Representative samples have been examined by petrographic microscopy and analyzed for major element glass composition by Electron Microprobe at the University of Hawaii (see Table 1 notes and ESM_2 for analytical details).

3.0. Dacite flow distribution and character

3.1 Distribution and general characteristics

The dacite lava flows occur in the rear arc, within a roughly triangular corridor between the NELSC on the west (German et al. 2006), the Mata boninite volcanoes to the northeast (Resing et al. 2011; Rubin and Embley 2012), the northernmost Tofua magmatic arc on the east, and Niuatahi Seamount, a large silicic submarine volcanic caldera, on the southern end of the corridor (Figs. 1-4). The volcaniclastic apron of the arc impinges on the area in the SE corner of the corridor. We refer to each geographically distinct site as a "lava flow field" because we cannot, with any certainty, resolve individual lava flows within them. In some places the word "lava flow" will be used in describing a morphologically distinguishable subunit within the lava flow field. The fields are named "Lau Lava" (LL), A, B, C, D from south to north. All three of the northern lava flow fields (LL-B, LL-B1, LL-C, and LL-D), which we will henceforth refer to as the "northern flow fields" when referring to the group, and the two largest Niuatahi flank fields (LL-A1 and LL-A3) have been sampled by dredge (Fig. 4). Only the LL-B and LL-C lava fields have been imaged by the TowCam (in 2010). All of these northern flow fields are

associated with the summit or flanks of a feature we call "Niuatahi Ridge", a diffuse shallow zone extending north from Niuatahi (Figs. 2-4).

188

189

190

191

192

193

194

195

196

197

198

199

200

201

202

203

204

205

206

207

208

209

210

We determined the extent of these lava flow fields on the basis of (higher) multibeam sonar acoustic backscatter intensity and, in most cases, on seafloor morphology (Figs. 2 and 3). Backscatter intensity is a function of slope, seafloor roughness, and acoustic impedance of the seabed. Most of the lava flow fields have been emplaced onto low regional slopes ($< 5^{\circ}$), so they can usually be distinguished from scarps that can also generate higher amplitude backscatter patterns. Most of the areas mapped as lava flows (Table 2) in this study also have small-scale topography resolved on the multibeam bathymetry (within a 20 m grid cell size) that is similar to features found in submarine and subaerial lava flow fields, including convoluted flow edges, depressions, pits and channels (Fig. 5) discussed in detail in later sections. Lower amplitude (m's), short wavelength that contributes to the backscatter signal is not resolved with the multibeam bathymetry (see below). One key point in interpreting backscatter is that there is a relationship between sediment cover and surface roughness. For example, sediment is differentially accumulated in pockets on a rough surface and as a blanket on smooth surfaces, so that more sediment accumulation is needed to completely obscure the microtopography in the former case. Thus, an originally smoother lava surface can appear to be "older" (lower backscatter) than a rougher lava surface of the same age. There is some variation in the backscatter intensity over the flow fields. In general, the northern flow fields have higher values versus the southern (Niuatahi fields) with the exception of LL-A3. The volcaniclastic apron of the Tonga arc is clearly defined by low backscatter on the southeast quadrant of the map. The lower backscatter values on the southern lava fields could be due to infiltration of fine volcaniclastic sediment (Figs. 2 and 3).

3.2 Lava samples characteristics and compositions

211

212

213

214

215

216

217

218

219

220

221

222

223

224

225

226

227

228

229

230

231

232

233

Most lava samples are sparsely vesicular (<1-3%) with elongate bubbles (1-5 mm in the long direction); samples collected from deeper regions of the lava flow fields (2.6 to 2.8 km water depth) have fewer vesicles than shallower ones (2.0-2.3 km water depth). Samples are sparsely phyric (<1%) with plagioclase laths up to 1 mm in length (with rare occurrences of crystals up to 5 mm in length) \pm pyroxene microphenocrysts (<1%). The groundmass varies from entirely glassy to microcrystalline (ESM 3), with unusually thick glass rinds (15-50 cm thick) (Figs. 6a and b). Many samples that preserve the upper lava flow surface have complex striated patterns, including a distinctive lineated texture we referred to at sea as "buffalo head hair", with subparallel wavy strands of glass forming the outer rind of the sample. We interpret these as local flow extrusion textures, ranging in wavelength from sub cm to several cm, in patches up to 10 cm long on hand samples (e.g., Fig. 6c). Although samples are generally glassy, some have whitish films on exterior surfaces and along internal cracks, although they are otherwise fresh on interior surfaces (Fig. 6). The TAS (total Alkali and Silica) diagram for all NE Lau silicic lavas (Fig. 7a) shows that all samples of the three largest northern high backscatter lava flows separated from Niuatahi (LL-B, LL-C, and LL-D) are dacite with an $SiO_2 \approx 65-68$ wt%. These flows have distinct compositions (warm colored symbols on Fig. 7, Table 1) compared to those associated with the Niuatahi caldera floor, along the ring faults, and on the presumptive youngest Niuatahi lavas on the Motutahi cone near the center of the caldera (cooler colored symbols on Fig. 7). The northern lava flows are also distinct from most of the (poorly sampled) flank lava flows LL-A1 to A5, most of which are also dacite, but with a broader compositional range than the northern flows (described in more detail below). An analysis of one dredge sample from LL-A1 (KM1129-D13-

R02) and one from LL-A3 (KM1008-D03-R01) were distinct from the northern lava trend (Figs. 234 235 4 and 7). However, analyses of two subsamples of dredge KM1129a-D15 (Table 1), taken on the 236 shallow area of LL-A3, had compositions within the tight field of the northern lavas. 237 The samples from the northern flow fields have a tight range of SiO₂, on average 66.17% 238 with $\sigma = 0.60$ wt% (with σ the population standard deviation). The LL-B field, which has the 239 largest aerial extent and the most dredges (six), has the tightest SiO₂ range with an average of 240 65.9% and $\sigma = 0.40$ wt% (Fig. 7a and Table 1). Expanded Harker diagrams for Al₂O₃, MgO and 241 FeO are shown, respectively, in Figs. 7b-d. Pseudo-Harker diagrams for, respectively, TiO₂ and 242 CaO/Al₂O₃, versus MgO are shown on Figs. 7e and 7f. The LL-B, LL-C and LL-D lava fields are 243 all very similar and form tight coherent clusters in all diagrams. Niuatahi itself, as well as the 244 LL-A1 and LL-A3 fields on the outer flanks of the volcano, are on trends extending from that 245 tight cluster to more differentiated compositions. 246 The coherence of the northern flow fields to a single compositional family with a small 247 range is quite evident in all the major element plots shown in Fig. 7. The northernmost dredge 248 sample, on LL-D (KM1024-D24, red diamond) is indistinguishable from the main big flow (LL-249 B) field (dark orange diamonds). The two dredges on the LL-C field (light orange) are slightly 250 more differentiated but on the same trends. Only one dredge not taken within the northern lava 251 flows, KM1129a-D15 from LL-A3, lies within their compositional field. Interestingly, this is 252 placed within the compositional field of LL-B, whose southwester boundary occurs about 20 km 253 to the northeast. The one dredge from the LL-A1 lava field south of Niuatahi (KM1129a-D13), 254 dredge KM1024-D03 from LL-A3, and both our dredge samples and those samples reported by 255 Park et al. (2015) from the caldera and its walls are all significantly different (i.e., more 256 differentiated) from the northern flow fields.

Flat MgO and FeO trends versus SiO₂ in the northern flow fields (LL-B, C, D) and a positive slope of Al₂O₃ versus SiO₂ in the northern flow fields are distinct from the Niuatahi samples (Figs. 7b-7d). Also of note is the tight TiO₂ vs. MgO (Fig. 7e) vertical trend and very highly clustered CaO/Al₂O₃ vs. MgO (Fig. 7f) of the northern flow fields, both of which are (also) distinct from the Niuatahi samples. It is difficult to make these (LL-B, C, and D) trends and the broad dispersion of the Niuatahi lavas from the same parent melt (see for instance the synthetic differentiation trajectories in ESM_4, which start with West Mata boninite as a parent). In addition, the small but identifiable differentiation trends for the northern flow fields (e.g., positive Al₂O₃ and Total alkalis vs. SiO₂ trajectories and flat MgO and FeO vs. SiO₂ trajectories) contrast with the trend for Niuatahi proper, suggesting different conditions of differentiation and crystallizing assemblage for the northern flow fields compared to Niuatahi. These parent melt and differentiation differences support the notion that the northern flow fields were probably not derived from the Niuatahi magma chamber.

Based on this, although we cannot completely rule out the possibility that the magma that fed the large northern flow fields came from beneath Niuatahi (e.g. the similarity of composition between one dredge from the LL-A3 lava and the LL-B compositional field), the case is not strong. Instead, given the significant differences from Niuatahi on most petrologic diagrams for all but the one LL-A3 dredge, we think that the parent magma for the northern flow fields is distinct from the Niuatahi source.

3.3 Niuatahi and LL-A lavas

Niuatahi seamount is ~21 km in diameter and is characterized by one of the largest submarine calderas (~9 km diameter) discovered to date (Kim et al. 2009). Active hydrothermal venting occurs in several places within the caldera and on the post-caldera Motutahi dacite near

281

282

283

284

285

286

287

288

289

290

291

292

293

294

295

296

297

298

299

300

301

302

its center (Kim et al. 2009; Resing et al. 2010). Dacite lavas have been recovered from both the caldera floor (~1800 m) and the young cone (Motutahi) (summit at ~1245 m) within the caldera. Rhyolites have been dredged from the ring structures forming the caldera walls (Figs. 4 and 7; Tables 1 and ESM_1) (Falloon et al. 2007; Park et al. 2015) and the present study. The age of the caldera-forming eruption is not known, but the multiple active hydrothermal sites within the caldera (Kim et al. 2009; Resing et al. 2010), very young dacite flows on the young cone (Motutahi) and within the caldera (unpublished data) and the high backscatter over the entire seamount (Fig. 3), imply that Niuatahi is an active volcano.

The LL-A series of high backscatter zones are located on the outward sloping flank of Niuatahi, and do not include obvious ridges or other regions of steep slopes such as the upper flanks of Niuatahi. These flow fields have an estimated area of ~166 km² (Table 2). All of these higher backscatter zones are contiguous to Niuatahi, and appear to have been sourced from the volcano or from structures related to the volcano. Their upper boundaries cannot be mapped in detail because they merge with the steep outer slope of Niuatahi. Only two of the Niuatahi flow fields (LL-A1 and LL-A3) have been sampled by dredge (Fig. 4) and all three dredges were dacite (see section 3.2), so we presume that the others have a similar composition. There is also the possibility that one or more of them (e.g., LL-A2) could be volcaniclastic flows, debris from sector collapse or some hybrid thereof. We surmise that the LL-A deposits were produced either coeval with, or postdate, caldera formation because one or more large paroxysmal eruption(s) would have produced eruptive products covering over the surface of pre-caldera flank lavas, which is not observed. Lavas have also erupted within the caldera of Niuatahi. A camera sled track over the young cone (KM1008 in May 2010) and a submersible dive in 2012 (on cruise RR1211 using the MARUM Quest 4000 ROV) imaged and sampled a dacite flow on the flank

and near the summit of the Motutahi cone in the SE part of the caldera (Fig. 2), as well as copious sulfur-rich emissions and solidified patchy yellow sulfur deposits near the summit.

Field LL-A3 has the highest backscatter of the Niuatahi flows, similar to the values on the northern flow fields (Fig. 3). The multibeam bathymetry (Fig. 8) shows that several lava flow units can be distinguished within the LL-A3 field. The northernmost and largest of the morphologically distinct lava flows (triangular-shaped area that cross-section A-B is centered on in Figure 8) originates from the elbow between Niuatahi and a short (~10 km) north rift zone extending from where the ring structures of Niuatahi have been partially breached (Fig. 2). This flow consists of a series of lobes extending into deeper water to the west. Its upper lobe (<2540 m) is at least 50 m thick and has small (\leq 10 m) domes and ridges on its surface. The deeper portions of the LL-A3a lava flow has a more irregular surface morphology with a series of interconnected lattice-like structures of ~10-15 m relief. The length of the field measures ~6 km from its western toe to its probable source near the summit of the ridge.

Although the LL-A3a unit was not sampled, two dredges further south on the flank of Niuatahi within LL-A3 (KM1004-D03 and KM1129a-D15; Figs. 4 and 8) sampled the upper portion of separate flows emerging from the northern rim of Niuatahi (Fig. 8). These samples are dacite (Table 1) but of measurably different composition (see section 3.2). The chemical similarity between the KM1024-D03 sample and the northern flow field compositional fields could represent a linkage between magma sources but it is difficult to draw a definitive conclusion from one sample location. The small low backscatter area in the middle of LL-A3 field is a kipuka defining the area where the lava flows comprising the LL-A3 field did not quite merge.

The high reflectivity zone on the southern flank of Niuatahi (LL-A1) has a mostly smooth surface on its deeper (SW) portion with higher relief topography on the shallower (closer to the caldera) portion where dredge KM1129-D09 recovered dacite lavas (Fig. 2 and 4). Although there is high backscatter over the entire region (Fig. 3), and some high relief areas that might be flow fronts, much of the deeper (unsampled) zone has low surface relief (~5 m).

We also interpret two other high-backscatter areas on the flanks of Niuatahi as lava flows because of their convoluted lower boundaries (A4, and A5). However, there are no samples from these areas so we can't rule out the possibility that some of these areas could be composed at least partly of slump material or volcaniclastic deposits.

3.4 LL-B lava flow field

The largest LL flow field, designated as LL-B, lies northeast of Niuatahi within the southwest corner of the rift basin that contains most of the Mata volcanoes (Figs. 2-4, and 9). This field has the largest area (~144 km²) of any of the lava fields discussed in this paper (Table 2), is the most densely sampled (KM1024-D06-D11), and has two camera tows on its western (shallower) side (Fig. 9c; CT-01 and CT-02). A much smaller but (apparently) separate lava flow (LL-B1) with an area of ~11 km² lies to the south of LL-B and is unsampled. A series of irregular rounded knolls on the summit of Niuatahi Ridge (Figs. 2 and 9a), upslope of LL-B and LL-B1, are up to ~200 m in height and 4 km in diameter. Several have enclosed deep depressions whereas others have a flat top with steep flanks, which stand out on the slope map (Fig. 9b). They follow an arcuate pattern from NW to SE mirroring the overall shape of the upper limit of LL-B. They have low backscatter values and, where imaged (beginning of CT-02 described below), their surface is smooth sedimented lava. We interpret these (as yet unsampled) features as silicic lava domes and coulees because of their geographic proximity to the silicic

349

350

351

352

353

354

355

356

357

358

359

360

361

362

363

364

365

366

367

368

369

370

volcano Niuatahi and the dacite lava fields, and their overall morphology and smooth surface. There is also a suggestion that they are part of a zigzag pattern of related hill and ridges extending northeast and then northwest from the eastern flank of Niuatahi (Figs. 2 and 9). To the ENE of the northwest trending "leg" of these hills, the LL-B and LL-B1 lava flow fields extends for ~10 km downslope and ~15 km in a NW-SE direction. The upper section of the LL-B flow field is defined by a depth range of ~2475-2500 m (level I on Fig. 9c) with a relatively low relief on a local scale with one exception, a 2 x 1.5 km, 30-m deep depression in its northern section (marked "LD" on Fig. 9). The morphology of the LD (size, steep walls, and flat floor; Fig. 10a) is similar to pit craters floored by frozen lava lakes on subaerial shield volcanoes (discussed in the following paragraph). There is also an apparent lava channel on the upper portion of the southern area of Level I (location of "LC" on Fig. 9). The LL-B flow field deepens in a series of steps (levels II-V) into the Mata basin bounded by sinuous (in plan view) high relief (20-80 m) scarps, which we interpret as lava flow fronts (Fig. 9c, profile A-B inset). The flow fronts within LL-B, defined by curvilinear (in plan view) steep slopes, have a lobate pattern that narrow downslope, providing an indication of flow direction at the time of emplacement. Although local flow directions vary, the overall pattern of these lobes suggests multiple sources curving around the southwestern slope of Mata basin. For example the relatively flat surface of the lobe northeast of the lava depression (near "III" on Figs. 9c) appears to have erupted along a SW-NE line and flowed mostly northwest. Also notable is the lining up of the SW-NE edge of this lobe with the long axis of the LD. The northeastern edge of LL-B is marked by a sharp contrast in backscatter within hundreds of meters northeast of the scarps. Two traverses with the TowCam (Figs. 9c; Figs. 10a and 10b) were made on the upper

surface (Level I) of LL-B. The camera tows overlap with dredge tracks so we are confident that

372

373

374

375

376

377

378

379

380

381

382

383

384

385

386

387

388

389

390

391

392

393

the lava flow images represent flows with a dacite composition. The primary objective of camera tow CT-01 was to traverse the floor and walls of the LD. It began imaging the seafloor about 0.5 km west of the west rim of the LD in a water depth of ~2495 m, descended onto the floor of the LD (~2530 m) and traversed N-NNE along the floor to within about 0.5 km of the northeastern rim (Fig. 10a). The camera contacted the seafloor during the first few minutes of the tow west of LD, apparently having descended into a local 5-10 m steep-walled lava pit or blocky area (Fig. 10a, inset). Photos from this portion of the tow show closely spaced horizontal bands on the wall of the pit (Fig. 11a). Two possible explanations for these lineations are: (1) "bathtub rings" found on drained out lava lakes on the mid-ocean ridge, which record the level of the subsiding lava pond as it drains out (Ballard et al. 1979; Chadwick 2003), and (2) lineations characteristic of crease structures on silicic lava domes and flows formed by progressive cracking and extrusion along a spreading structure (Anderson and Fink 1992). The west rim area of the LD is mostly of rounded pillows and flatter lobate forms with some brecciated ropey flows in places (Fig. 11b). Images of the west wall of the depression show a near-vertical scarp, consistent with both the multibeam and camera tow bathymetry (Fig. 10a, inset). The floor of the LD consists of low relief (~10 m across 2 km) sedimented lava breccia. Most of the lava breccia appears to be flow breccia, probably from broken up ropey flow. However, there are a few areas where large intact ropey lava flow folds were preserved (e.g., Fig. 11c), so the ropey surface is apparently the upper surface of extensive low viscosity lava. The nearly flat floor of the depression is similar in morphology to the floors of drained-out lava lakes on the mid-ocean ridge (Ballard et al. 1979) and lava lakes on subaerial volcanoes. This frozen "lava lake" could have formed directly over the magma conduit as the lava drained through subsurface tubes. Another possibility is that LD is a type of perched lava pond such as have been described from Kilauea eruptions (Wilson and

Parfitt 1993). However, perched lava ponds are rootless features with a maximum of 100s m diameter and a few meters relief, compared to the 2 x 1.5 km diameter of the LL-B depression, so we favor the drained lava lake explanation.

394

395

396

397

398

399

400

401

402

403

404

405

406

407

408

409

410

411

412

413

414

415

416

Camera tow CT-02 (Fig. 10b) began on the east side of the sedimented dome on the upper reaches of the northwestern sector of LL-B and traversed downslope and crossed into and then traversed the LL-B field for about 2 km. The first part of the tow (not shown on Fig. 10b, inset) traversed over heavily sedimented terrain with some outcropping substrata that appear to be lavas. The backscatter boundary coincides with an abrupt transition (at ~2590 m) into thinly sedimented lavas displaying a range of morphologies. Many of the images show anastomosing pillow tubes, sometimes flowing down gentle slopes for tens of meters (Fig. 11d), and in some places flowing amidst blocky ridge or dome-like structures (Fig. 11e; ESM 5). The pillow tubes often terminate with ballooning extrusions that can produce a spiny mass (Fig. 11f) or split and extrude into three sections (Fig. 11g). Interspersed within the pillow flows are domes and ridges with 10-100 m scale that show a variety of surface textures and structures. In some places, a series of cracks occur on otherwise smooth lava, presumably formed by extension of the flow surface during eruption (Fig. 11h). There are also fractured structures covered with broken folded ropey flows similar to those seen on CT-01 in the LD (Figs. 11i and j). Many of the ridges have axial fractures that can sometimes occur in a triaxial pattern (Fig. 11k). In some cases, the higher relief structures have smooth surfaces that have probably opened by endogenous growth creating linear features that appear to be extrusion structures resembling the "crease" structures observed in low viscosity subaerial (Anderson and Fink 1992) and some submarine inflated basaltic lava flows (Appelgate and Embley 1992) (Fig. 111). Some of the inflated/fractured ridges and domes have onlapping pillow lavas suggesting multiple eruptive pulses (Fig. 12a).

3.5 LL-C lava flow field

417

418

419

420

421

422

423

424

425

426

427

428

429

430

431

432

433

434

435

436

437

438

439

The LL-C lava field, the third in size of the northern flow fields (total area of ~26 km²), is an inverted v-shaped area of high backscatter centered on the crest of the Niuatahi Ridge and extending to the SW and SE on, respectively, the western and eastern flanks of the ridge (Figs. 2-4). The western flank field is a hummocky terrain aligned within a SW-NE oriented band that separates from the main ridge to the south. The irregular hummocky terrain implies short run out distance, so the flows were probably volume limited (Fig. 10c). Camera tow CT-05 traversed from west to east up and over these hummocky flows. After traversing thickly sedimented, presumptively older, lavas outside of the LL-C backscatter boundaries, the camera passed over the northern terminus of the southern flow (near "SF" Fig. 10c), which consisted of mixed tubular and flatter lobate pillows punctuated (Fig. 11m and 12b) by extrusion structures forming the end of the pillow flow (Fig. 11n; ESM 6). The camera then passed up and over the 40-50 m high northern flow ("NF" on Fig. 10c) (near dredge KM1024-D04) where it imaged more pillows, including some with the peculiar "buffalo head hair" surface texture (Figs. 7 and 110), which is common on dredged samples of the northern flow fields. The top of the NF has smooth areas, including domes and ridges with large tensional fractures, which are common on inflated lava flow structures. In some cases the underlying massive flow's columnar jointing was exposed, probably as the lava was domed and fractured by endogenous growth (Fig. 11p). 3.6 LL-D lava flow field The LL-D lava field abuts the heavily-sedimented (low backscatter) fractured Niuatahi Ridge north of LL-C (Fig. 2). The axis of the NELSC lies to the west. This field has the most

Without groundtruthing, however, it is not possible to determine whether the higher backscatter

uniformly high backscatter of all the northern flow fields and is second in area at 55 km².

represents a younger (less sedimented) or a less rugose surface. However, this lava flow field is farthest in distance from direct pathways of volcaniclastic sediment transport from the magmatic arc, which is consistent with a thinner sediment cover than the young lava fields that lay to the south. The lava flow surface increases in depth from south to north in a series of steps (I-IV on Fig. 13) whose surfaces have numerous small depressions and ridges. Most of the flow fronts are broad or stubby, but there is one well-defined sinuous lava flow with an along-axis length of ~1.75 km ("a" on Fig. 13) and a relief (thickness?) of 40-60 m. The deeper lava surfaces (II and III) have numerous 5-10 m irregular-shaped pits on them. Some of the depressions, e.g., the ones on surface III ("b" on Fig.13) may have also formed by lava drainout. The scarps defining the outer limits of the various levels of LL-D, which we assume are flow fronts, vary from ~30-60 m, similar to the thickness of the "a" lava flow. A large open channel-like feature one km in width and several km long extends northwest into the valley to the west ("c" on Fig. 13). This channel drops ~300 m into hummocky terrain that could be lava flow fronts. The channel likely formed when the lavas reached a steeper (faulted) slope into the rifted terrain to the west.

The eruption source for LL-D is unclear. A large mass of the lavas appear to have flowed north parallel to the regional structure, forming successively deeper levels of the lava surface. However, some of the shallower high-backscatter terrain is contiguous to the faulted structure to the east with some of the lobes deepening to the west. There could be multiple lava sources along the ridge. The LL-D flow field has only one dredged sample set (KM1024-D24 taken within the large channel, Fig. 13), and it is compositionally indistinct from the northern flow fields (LL-B and LL-C).

4.0 Discussion

Although we have presented the setting, morphology and composition of these flows in as much detail as our data sets allow, our interpretations are necessarily limited by the lack of detailed seafloor (optical) imagery, near-bottom high resolution bathymetry, and high density rock sampling, such as is more easily accomplished for terrestrial lava flows. Our sampling is limited and non-uniform so, for instance, we don't know the composition of volcanic products from the intervening areas, between the lava fields. In some ways the level of field study presented here is akin to the early studies of large continental composite volcanoes. In this section we make certain inferences with the present data set and present some hypotheses to be tested in the future.

4.1 Sources of erupted magmas

We divide the dacite lava fields into two main categories, those erupted on the flanks of and/or in proximity to Niuatahi (LL-A1-A5) that are likely erupted from its underlying magma chamber, and those located north of and geographically separated from the volcano. The compositional variation of the northern lava flows is narrowly constrained in major elements whereas the Niuatahi lavas have a wider range, although the latter is poorly sampled (as discussed in section 3.2).

The northern flow fields are of particular interest because of their extent and that they are not clearly related to a major constructional volcanic feature (e.g., spreading center, central volcano). The northern flow fields all occur in a north-south corridor containing some north-south striking structures, including a short (~10 km) rift zone and ridge extending north from Niuatahi. Thus it is tempting to propose that these northern flow fields erupted from dike injections issuing from the magma chamber beneath Niuatahi and extending along the axis of

this region, perhaps associated with caldera-forming paroxysmal event. Along-axis diking events are common at basaltic shield volcanoes such as Kilauea (Epp et al. 1983), Icelandic central volcanoes such as Krafla (Einarsson 1991; Buck et al. 2006), Askja (Sigurdsson and Sparks 1981) and on submarine volcanoes such as Axial seamount (Juan de Fuca Ridge) (Dziak and Fox 1999), and on the mid-ocean ridge (Einarsson 1991; Fox et al. 1995; Embley and Lupton 2004). However, in all these cases mafic magmas were involved. Silicic dikes exist as well (Fink 1985), but their ability to propagate for distances longer than a few kilometers has not been well documented. A lateral dike injection would imply a dike of between 30 and 60 km (from the center of Niuatahi to the southern and northern boundaries of LL-D). Also, the chemistry of the northern flow field lavas is not generally consistent with their being erupted from a dike originating from the Niuatahi magma chamber (see section 3.2).

Alternatively, the dacite lavas could be a differentiate of the boninite magma that erupted in the nearby Mata basin. A differentiated series of Miocene boninitic lava has been well-documented on Chichi-jima (Bonin islands) and within nearby dredged and drilled sections (Bloomer and Hawkins 1987; Taylor et al. 1994) and a similar case has been made for older dredged rocks in the NE Lau basin (Falloon et al. 2007). The very low TiO_2 contents of the dacites reported here $(0.60 \pm 0.05 \text{ wt. \%})$ is consistent with this scenario. There is no trend at all of Fe_2O_3 or TiO_2 vs. SiO_2 in the northern dacites (in fact both don't vary with changes in SiO_2 or with each other) indicating that the low TiO_2 is not due to Fe-Ti-oxide fractionation. Analyses of recently obtained trace element data for the current suite of samples should shed light on this hypothesis (Rubin et al. 2015). However, this scenario requires a location near the locus of boninitic volcanism to store, differentiate and compositionally homogenize magmas before eruption.

If the northern dacite lavas (LL-B, LL-B2, LL-C and LL-D) are differentiated from boninite magmas, and had a magma source separate from Niuatahi, one also has to explain the spatial distribution of the boninite and dacite lavas and apparent lack of inter-fingering. Although the dacites are all centered around and partly on the summit of N-S ridge structures, there are also other regional structures that could influence lava plumbing. Most striking are those along a SW-NE trend, following the trend of rift zone of West Mata and southernmost of the smaller Mata volcanoes (Fig. 2). Similar trending structures appear to control some of the volcanic ridges around Niuatahi (most obvious in the area SW of the caldera) (Fig. 2). An historic eruption occurred along an extension of the southwest rift zone of West Mata (yellow patch with black outline below "West Mata" label on Fig. 9) (Embley et al. 2014) but it has not yet been sampled. There are also apparent SW-NE trends on the LL-B lava, including the elongation of the lava depression and the edges of some of the deeper flows (Fig. 9). The western portion of LL-C is also aligned approximately in the same direction. So it is possible that the northern flow fields are controlled by intersecting N-S and SW-NE crustal fractures.

Overall, the dacite volcanism is apparently restricted to the most rapidly opening part of the NE Lau basin, along tectonic lineaments, in the basins near the northern edge of the region and near the currently subducting slab. The dacite volcanism also approximately coincides with the area near the edge of the active tear fault formed by the northern termination of the Tonga subduction zone at ~15°S The eruptibility of melts can be dependent on tectonics as well as buoyancy, which is apparent in subaerial settings such as the Inyo Domes-Mono Craters eruptions in California (Bursik et al. 2003). Tests of these hypotheses await results of future field studies.

The total area of all the silicic flows is ~402 km², including ~236 km² for the northern flow fields and ~166 km² estimated for the southern flows associated with Niuatahi, although the latter might include other types of volcanic flows (Table 2). However, it is not clear that all the areas mapped as lava flow fields around Niuatahi are lavas versus other types of volcanic flow (see section 3.3). Measurement of the volume is problematic, but, at least for the northern flow fields, our estimate is ~2.4-7.2 km³ (based on 10-30 m average relief of the flow fronts). With typical eruption rates for dacite lavas in subaerial environments, the NE Lau flows would have taken years to erupt. However, these flows exhibit a wide range of morphology (see next section), which is likely to be at least partly due to variable eruption rates, potentially allowing for a shorter eruption duration.

4.2 Submarine dacite lava regimes

The multibeam data provide a first-order morphology map of the lava flow units, but do not have sufficient resolution to discriminate individual lava flows or small scale morphology (meters to tens of meters). The camera tow images provide some information on small-scale structures, but are very limited in the area they cover, ~0.04 km² total area compared to the several hundred square kilometers of the lava flows. The available imaging reveals lava flows with an almost complete overlap of lava regimes found in submarine basaltic lava flows, including ropey, pillow and inflated flows. Different lava regimes often onlap one another.

Both compressional and tensional surface features are observed on subaerial lava fields – this duality apparently modulated by the effusion rate (Blake and Bruno 2000; Lescinsky 2005). Fracture patterns such as the "tri-cracks" (fractures, sometime acting as loci of extrusion, oriented at spacing of ~120°) are similar to those found on subaerial lavas and submarine lavas formed during endogenous growth are common (Walker 1991; Appelgate and Embley 1992;

Hon et al. 1994). Groups of extensional fractures, such as those found oriented perpendicular to the flow direction on subaerial flows, can also occur as the upper section of the flow stagnates and lower part advances.

554

555

556

557

558

559

560

561

562

563

564

565

566

567

568

569

570

571

572

573

574

575

576

Lava pits and depressions found on the surface of LL-B and LL-D suggest high eruption rate, and relatively low viscosity eruptions. The LL-B lava depression has the size and morphological character (e.g., flat floor) of lava lakes formed directly over a primary lava conduit (e.g. Kilauea). The LD is surrounded by a low-relief area extending out for up to ~2.5 km with radial trough dipping in towards the center. To our knowledge such a feature has never been described, neither for subaerial nor for submarine silicic eruptions. The lavas associated with the LD, such as the ropey forms observed on CT-01, are consistent with low viscosity eruptions and high effusion rates, possibly due a higher temperature than usually associated with dacite magma. It is tempting to think of the LD region as a "silicic shield" formed during the eruption of a low viscosity submarine dacite flow that is unlikely to ever form in the subaerial environment. High eruption temperatures, rapid emplacement and subsequent rapid cooling are consistent with the very glassy to mildly microcrystalline groundmass of most lava samples from the dacite flows. High dissolved water contents can lower the viscosity (Spera 2000) of lavas of a given composition. Dacite and rhyolite lava flows in subaerial environments are usually thick and erupted at a high viscosity, generating lavas with short run outs. Yet submarine dacite lavas at these water depths (~2400-2800 m) erupted from magmas with presumptive high dissolved volatile contents high temperatures, and with sparsely phyric texture could, theoretically, be derived from the lowest end of the viscosity scale for melts of their chemistry range, perhaps as low as $\sim 10^{-3}$ - 10^{-4} Pa·s, which is within the range of viscosities for typical andesites (Takeuchi 2011; Takeuchi 2015).

Furthermore, experimental work by Whittington et al. (2009) on hydrous dacitic melts show that, even at typical liquidus temperatures (for the given composition), dacitic melts are only slightly more viscous than andesitic melts (a larger increase is associated with rhyolite composition). The suite of dredged samples from LL-B, LL-C and LL-D show limited vesiculation, even in those samples in the shallower (near-vent?) regions of the LL-B flow field (D06 and D07). Also, they are nearly aphyric, which is consistent with higher temperatures and a lower viscosity.

An important inference from this study is that the morphology of these silicic submarine lava flows almost completely overlap basaltic submarine lavas, which are much better studied. The lava depression on LL-B appears to contain a frozen lava lake of dacite, formed during a high effusion rate episode that ended with the drainout of the lava creating a 30 m deep, 2.0 x 1.5 km depression. Similar depressions are found on LL-D, including a possible breached feature of comparable size to the LL-D depression.

Gregg and Fornari (1998) concluded that submarine basaltic lava flows have the potential for greater flow lengths, mostly due to better insulation from formation of a thick glassy layer not found on subaerial flows. The glass layer for the dacites is about 10 to 100 times as thick as that of a submarine basalt (10s of cm vs. 0.1 to 1 cm), offering an even greater insulation effect. High effusion rates, high liquidus temperatures and high gas retention are the conditions for relatively low viscosity geomorphology of portions of the Lau dacite lava flows. However, a cautionary note is that we have very limited high resolution imagery on these dacite lava fields. Even the existing photographic transects show a wide range of flow regimes, and we have no detailed imaging of the deeper portions of the LL-B (where there are high relief flow fronts), and

none over the entire LL-D flow field. More detailed field work is needed to resolve the range of flow regimes and rheological evolution of a deep submarine dacite eruption.

4.3 Silicic submarine lavas in the ancient record

599

600

601

602

603

604

605

606

607

608

609

610

611

612

613

614

615

616

617

618

619

620

621

Knowledge of other submarine silicic lavas is mostly confined to rare ancient sequences exposed on land and to small batches of evolved lavas present within mid-ocean ridge and transform environments, so the NE Lau dacite flows provide the first look at young, aerially extensive, large volume, deep submarine silicic lava flows on Earth. Because of their setting within the world's fastest backarc opening rate intra-oceanic subduction zone and consequent high upper mantle temperatures, the NE Lau basin should potentially provide some new insights into magmatic processes operative in early Earth with its higher heat flow gradients. The production of extensive, geographically contiguous, boninite eruptions is additional evidence for regionally high upper mantle temperature melts here and slab-derived volatile fluxes. The higher upper mantle temperature could yield lavas with higher eruption temperatures for a given magmatic composition, leading to lower than normal viscosities. There are no equivalents in the literature on modern subaqueous dacite lava flows comparable to the observations described here and only a few cases of (apparently deep) submarine dacite lavas have been reported in ancient rock sequences now exposed on land. Extensive pillow like forms of submarine dacite lava reported from the Archaean of Ontario, Canada (Dinel et al. 2008) with at least the run out length of the Lau layas (~10 km). Dinel et al. (2008) propose that the laya flows erupted in a "superheated" state, consistent with their aphyric nature. They speculate that this superheated state might have resulted from the higher geothermal gradients associated with the Archaean Earth (Langdon and Sleep 1982). Dacite to rhyodacite lavas pillows and tubes from the Ordovician of Wales are also ascribed to high effusion rate, high temperature eruption and

623

624

625

626

627

628

629

630

631

632

633

634

635

636

637

638

639

640

641

642

643

possibly a high slope angle (Bevins and Roach 1979). Cas (1978) reports on extensive andesite to dacite lavas in the Devonian/Carboniferous of New South Wales, Australia and invoked low viscosity resulting from deep water (high pressure) retention of volatiles. Finally, Gibson et al. (1999) emphasize the rarity of such extensive siliceous flows in the geologic record. Some deep-water dacite lavas from younger subaqueous sequences in island arc settings (exposed on islands and trench walls) are often geochemically associated with boninite lavas (Kuroda et al. 1978; Bloomer and Hawkins 1987; Kuroda et al. 1988; Dobson et al. 2006). Both major and trace element data suggest that the more evolved lavas derive from fractional crystallization of boninite magmas. **5.0 Conclusions** (1) Hundreds of square kilometers of young dacite lavas been mapped and sampled in the NE Lau basin, identifying the largest currently known submarine dacite lava occurrence on Earth. Several fields are flank flows from a silicic volcano (Niuatahi). The remaining three major flow fields (and one smaller field) occur 15-60 km north of Niuatahi within a corridor between the NELSC and the Mata boninite volcanoes and the Tofua arc. The northern flow fields are compositionally indistinguishable from each other, and distinct from the flows nearest Niuatahi. (2) The northern lava flow fields, which are geographically isolated from the lava fields associated with Niuatahi, cover ~236 km² and have thicknesses, at least in places, of ~10-30 m, yielding a volume of $\sim 2.4-7.2 \text{ km}^3$. (3) The geographic magmatic source of the northern flow fields is not clear. Either they erupted from long dikes generated at the silicic Niuatahi seamount to the south, or have tapped separate magma sources and erupted along crustal fractures. Chemical differences with Niuatahi lavas

645

646

647

648

649

650

651

652

653

654

655

656

657

658

659

660

661

662

663

664

665

666

favor a distinct source scenario, from a large, well-mixed magma body or bodies erupted along crustal fractures in the rear arc north of Niuatahi seamount. (4) Where imaged by camera, the dacite lavas have similar to indistinguishable range of morphologies compared to MORB lavas, including pillows and ropey flows. Deep submarine dacite lavas can have lower viscosities than subaerial equivalents because of higher volatile retention (due to high confining pressures) and in the Lau case, possibly higher eruption temperatures. The Lau basin, with its high upper mantle temperatures relative to other back arc basins, enhances the eruptibility of large volumes of silicic lavas. Acknowledgments. We are indebted to Susan Merle for her skillful processing and diligent management of our multibeam data sets and help with some of the figures. Sarah Glancy and Eric Hellebrand are thanked for preparing the sources and collecting the glass electron microprobe data described here. The science party of expedition KM1024 worked incredibly hard for 6 days to obtain the dredge samples reported on here, to help with sample selection and description, and for witty repartee (especially Richard Arculus), as did the science party of KM1129a, which collected dredge samples from Niuatahi. We also thank the officers, crew and shipboard technical group on the R/V Kilo Moana for their dedicated, 24 hour support during the dredging and camera operations. Chris Russo is thanked for assisting Rubin on the transit leg from Samoa to Honolulu following KM1024 with processing, describing and subsampling dredged lavas. Dan Fornari provided outstanding support for the TowCam setup operations on KM1008; K. Feldman and S. Hanneman kept the system operating at a high performance level at sea. The NOAA Office of Marine and Aircraft Operations provided funding for KM1008 and for part of KM1024. The University of Hawaii provided part of the ship time that made KM1024

possible and all of the funds for KM1129a (in part using funds donated by Nautilus Minerals,
Inc). The NOAA Office of Ocean Exploration, the NOAA Vents Program and the NOAA Earth-
Ocean Introduction program provided funding for RWE. KHR was supported by NSF OCE
0929881 and 1538121. R. Cas, an anonymous reviewer and associate editor PS. Ross provided
valuable comments that improved the final manuscript. PMEL contribution 4555 and SOEST
contribution 10058.

References Cited 687 688 Anderson SW, Fink JH (1992) Crease structures: indicators of emplacement rates and surface 689 stress regimes of lava flows. Geol Soc Am Bull 10(5):615-625 690 Appelgate B, Embley RW (1992) Submarine tumuli and inflated tube-fed lava flows on Axial 691 Volcano, Juan de Fuca Ridge. Bull Volcanol 54(6):447-458 692 Baker ET, Lupton JE, Resing JA, Baumberger T, Lilley MD, Walker SL, Rubin KH (2011) 693 Unique event plumes from a 2008 eruption on the Northeast Lau Spreading Center. 694 Geochem Geophys Geosyst 12(9). doi:10.1029/2011GC003725 695 Ballard RD, Holcomb RT, Van Andel TH (1979) The Galapagos Rift at 86 W: 3. Sheet flows, 696 collapse pits, and lava lakes of the rift valley. Journal of Geophysical Research: Solid 697 Earth 84(B10):5407-5422 698 Baumberger T, Lilley MD, Resing JA, Lupton JE, Baker ET, Butterfield DA, Olson EJ, Früh-699 Green G (2014) Understanding a submarine eruption through time series hydrothermal 700 plume sampling of dissolved and particulate constituents: West Mata, 2008–2012. 701 Geochem Geophys Geosyst 15(12):4631-4650. doi: 4610.1002/2014GC005460 702 Bevins RE, Roach RA (1979) Pillow lava and isolated-pillow breccia of rhyodacitic composition 703 from the Fishguard Volcanic Group, Lower Ordovician, SW Wales, United Kingdom. 704 The Journal of Geology 87:193-201 705 Binns RA, Scott SD (1993) Actively forming polymetallic sulfide deposits associated with felsic 706 volcanic rocks in the eastern Manus back-arc basin, Papua New Guinea. Econ Geol 707 88(8):2226-2236 708 Bird P (2003) An updated digital model of plate boundaries. Geochem Geophys Geosyst 4(3). 709 doi:10.1029/2001GC000252 710 Blake S, Bruno B (2000) Modelling the emplacement of compound lava flows. Earth Planet Sci 711 Lett 184(1):181-197 712 Bloomer SH, Hawkins JW (1987) Petrology and geochemistry of boninite series volcanic rocks 713 from the Mariana trench. Contrib Mineral Petrol 97(3):361-377 714 Buck WR, Einarsson P, Brandsdottir B (2006) Tectonic stress and magma chamber size as 715 controls on dike propagation: Constraints from the 1975–1984 Krafla rifting episode. 716 Journal of Geophysical research: Solid Earth 111(B12):B12404. 717 doi:12410.11029/12005JB003879 718 Bursik M, Renshaw C, McCalpin J, Berry M (2003) A volcanotectonic cascade: Activation of 719 range front faulting and eruptions by dike intrusion, Mono Basin-Long Valley Caldera, 720 California. Journal of Geophysical Research: Solid Earth 108(B8). 721 doi:10.1029/2002JB002032 722 Cas RAF (1978) Silicic lavas in Paleozoic flyschlike deposits in New South Wales, Australia: 723 Behavior of deep subaqueous silicic flows. Geol Soc Am Bull 89(12):1708-1714 724 Chadwick WW (2003) Quantitative constraints on the growth of submarine lava pillars from a 725 monitoring instrument that was caught in a lava flow. Journal of Geophysical Research: 726 Solid Earth 108(B11). doi:10.1029/2003JB002422 727 Chadwick WW, Clague DA, Embley RW, Perfit MR, Butterfield DA, Caress DW, Paduan JB, 728 Martin JF, Sasnett P, Merle SG (2013) The 1998 eruption of Axial Seamount: New 729 insights on submarine lava flow emplacement from high-resolution mapping. Geochem 730 Geophys Geosyst 14(10):3939-3968. doi:3910.1002/ggge.20202

Clague DA, Caress DW, Rubin KH, Paduan JB (2010) The 2010 Puipui eruption and
 morphology of Northeast Lau Spreading Center between Maka and Tafu. Abstract T11E 03 presented at 2010 Fall Meeting, AGU, San Francisco, CA

- Clague DA, Paduan JB, Caress DW, Thomas H, Chadwick WW, Jr., Merle SG (2011) Volcanic morphology of West Mata Volcano, NE Lau Basin, based on high-resolution bathymetry and depth changes. Geochem Geophys Geosyst 12. doi:029/2011GC003791
 - Clague DA, Dreyer BM, Paduan JB, Martin JF, Chadwick WW, Caress DW, Portner RA, Guilderson TP, McGann ML, Thomas H, Butterfield DA, Embley RW (2013) Geologic history of the summit of Axial Seamount, Juan de Fuca Ridge. Geochem Geophys Geosyst 14(10):4403-4443. doi: 10.1002/ggge.20240
 - Colman A, Sinton JM, White SM, McClinton JT, Bowles JA, Rubin KH, Behn MD, Cushman B, Eason DE, Gregg TKP, Grönvold K, Hidalgo S, Howell J, Neill O, Russo C (2012) Effects of variable magma supply on mid-ocean ridge eruptions: Constraints from mapped lava flow fields along the Galápagos Spreading Center. Geochem Geophys Geosyst 13(8). doi:10.1029/2012GC004163
 - Deschamps A, Grigné C, Le Saout M, Soule SA, Allemand P, Vliet-Lanoe V, Floc'h F (2014) Morphology and dynamics of inflated subaqueous basaltic lava flows. Geochem Geophys Geosyst 15(6):2128-2150. doi:2110.1002/2014GC005274
 - Dinel E, Saumur BM, Fowler AD (2008) Spherulitic aphyric pillow-lobe metatholeiitic dacite lava of the Timmins Area, Ontario Canada: a new Archean facies formed from superheated melts. Econ Geol 103(6):1365-1378. doi: 1310.2113/gsecongeo.1103.1366.1313
 - Dobson PF, Blank, JG, Maruyama S, Liou, JG (2006) Petrology and geochemistry of boninite-series volcanic rocks, Chichi-Jima, Bonin Islands, Japan. Int Geol Rev 48(8):669-701
 - Dziak RP, Fox CG (1999) The January 1998 earthquake swarm at Axial Volcano, Juan de Fuca Ridge: Hydroacoustic evidence for seafloor volcanic activity. Geophys Res Letts 26:3429-3433
 - Einarsson P (1991) Earthquakes and present-day tectonism in Iceland. Tectonophysics 189(1):261-279
 - Embley RW, Chadwick WW (1994) Volcanic and hydrothermal processes associated with a recent phase of seafloor spreading at the northern Cleft segment: Juan de Fuca Ridge. Journal of Geophysical Research: Solid Earth 99(B3):4741-4760
 - Embley RW, Lupton JE (2004) Diking, event plumes, and the subsurface biosphere at Mid-Ocean Ridges In: Wilcock WSD, DeLong EF, Kelley DS, Baross JA, Cary SC (eds) The Subseafloor Biosphere at Mid-Ocean Ridges American Geophysical Union, Geophysical Monograph 144, Washington, D. C., pp 75–97. doi: 10.1029/144GM06
 - Embley RW, Merle SG, Lupton JE, Resing JA, Baker ET, Lilley MD, Arculus RJ, Crowhurst PV (2009) Extensive and diverse submarine volcanism and hydrothermal activity in the NE Lau Basin. Abstract V51D-1719 Eos Transactions AGU, 90(52), Fall Meet. Suppl., p 1719
 - Embley RW, Merle SG, Baker ET, Rubin KH, Lupton JE, Resing JA, Dziak RP, Lilley MD, Chadwick WW, Shank T, Greene R, Walker S, Haxel J, Olsen E, Baumberger T (2014) Eruptive modes and hiatus of volcanism at West Mata seamount, NE Lau basin: 1996–2012. Geochem Geophys Geosyst 15(10):4093–4115. doi:10.1002/2014GC005387
- Epp D, Decker RW, Okamura RT (1983) Relation of summit deformation to east rift zone eruptions on Kilauea Volcano. Geophys Res Lett 10(7):493-496

- Falloon TJ, Danyushevsky LV, Crawford TJ, Maas R, Woodhead JD, Eggins SM, Bloomer SH,
 Wright DJ, Zlobin SK, Stacey AR (2007) Multiple mantle plume components involved in
 the petrogenesis of subduction-related lavas from the northern termination of the Tonga
 Arc and northern Lau Basin: Evidence from the geochemistry of arc and backarc
 submarine volcanics. Geochem Geophys Geosyst 8(9). doi:10.1029/2007gc001619
 - Fink JH (1985) Geometry of silicic dikes beneath the Inyo Domes, California. Journal of Geophysical Research: Solid Earth 90(B13):11,127-111,133

- Fiske RS, Naka J, Iizasa K, Yuasa M, Klaus A (2001) Submarine silicic caldera at the front of the Izu-Bonin arc, Japan: Voluminous seafloor eruptions of rhyolite pumice. Geol Soc Am Bull 113(7):813-824
- Fornari DJ, Haymon RM, Perfit MR, Gregg TKP, Edwards MH (1998) Axial summit trough of the east Pacific Rise 9°N to 10°N: Geological characteristics and evolution of the axial zone on fast-spreading mid-ocean ridges. Journal of Geophysical Research: Solid Earth 103(B5):9827-9855. doi:10.1029/98JB00028
- Fox CG, Radford WE, Dziak RP, Lau TK, Matsumoto H, Schreiner AE (1995) Acoustic detection of a seafloor spreading episode on the Juan de Fuca Ridge using military hydrophone arrays. Geophys Res Letts 22:131-134
- German CR, Baker ET, Connelly DP, Lupton JE, Resing J, Prien RD, Walker SL, Edmond HN, Langmuir CH (2006) Hydrothermal exploration of the Fonualei Rift and spreading center and the Northeast Lau spreading center. Geochem Geophys Geosyst 7(11). doi: 10.1029/2006GC001324
- Geshi N, Umino S, Kumagai H, Sinton JM, White SM, Kisimoto K, Hilde TW (2007) Discrete plumbing systems and heterogeneous magma sources of a 24 km³ off-axis lava field on the western flank of East Pacific Rise, 14° S. Earth Planet Sci Lett 258(1):61-72. doi:10.1016/j.epsl.2007.1003.1019
- Gibson HL, Morton RL, Hudak GJ (1999) Submarine volcanic processes, deposits, and environments favorable for the location of volcanic-associated massive sulfide deposits. In: Barrie CT, Hannington MD (eds) Volcanic-associated massive sulfide deposits-Processes and examples in modern and ancient settings: Reviews in Economic Geology. Society of Economic Geologists, Littleton, CO, pp 13-51
- Govers R, Wortel MJR (2005) Lithosphere tearing at STEP faults: Response to edges of subduction zones. Earth Plan Sci Lett 236(1-2):505-523. doi:510.1016/j.epsl.2005.1003.1022
- Graham IJ, Reyes AG, Wright IC, Peckett KM, Smith IEM, Arculus RJ (2008) Structure and petrology of newly discovered volcanic centers in the northern Kermadec–southern Tofua arc, South Pacific Ocean. Journal of Geophysical Research: Solid Earth 113(B8). doi:10.1029/2007JB005453
- Gregg TK, Fornari DJ (1998) Long submarine lava flows: Observations and results from numerical modeling. Journal of Geophysical Research: Solid Earth 103(B11):27517-27531
- Gribble RF, Stern RJ, Newman S, Bloomer SH, O'Hearn T (1998) Chemical and isotopic composition of lavas from the northern Mariana Trough: Implications for magmagenesis in back-arc basins. J Petrol 39(1):125-154
- Hon K, Kauahikaua J, Denlinger R, Mackay K (1994) Emplacement and inflation of pahoehoe sheet flows: observations and measurements of active lava flows on Kilauea Volcano, Hawaii. Geol Soc Am Bull 106(3):351-370

- Isacks B, Sykes LR, Oliver J (1969) Focal mechanisms of deep and shallow earthquakes in the Tonga-Kermadec region and the tectonics of island arcs. Geol Soc Am Bull 80(8):1443-
- Kim J, Son S-K, Son J-W, Kim K-H, Shim WJ, Kim CH, Lee K-Y (2009) Venting sites along the Fonualei and Northeast Lau Spreading Centers and evidence of hydrothermal activity at an off-axis caldera in the northeastern Lau Basin. Geochem J 43(1):1-13. doi: 10.2343/geochemj.0.0164
 - Kuroda N, Shiraki K, Urano H (1978) Boninite as a possible calc-alkalic primary magma. Bulletin Volcanologique 41(4):563-575

- Kuroda N, Shiraki K, Urano H (1988) Ferropigeonite quartz dacites from Chichi-jima, Bonin Islands: Latest differentiates from boninite-forming magma. Contrib Mineral Petrol 100(2):129-138
- Langdon RT, Sleep NH (1982) A kinematic thermal history of the Earth's mantle. J Geophys Res 87(B11):9225-9235
- Lescinsky DTM, Merle O (2005) Extensional and compressional strain in lava flows and the formation of fractures in surface crust. In: Manga M, Ventura G (eds) Kinematics And Dynamics of Lava Flows. Special Paper 396, Geological Society of America, Boulder, CO, pp 163-179
- Lonsdale P, Hawkins J (1985) Silicic volcanism at an off-axis geothermal field in the Mariana Trough back-arc basin. Geol Soc Am Bull 96(7):940-951
- Lupton J, Rubin KH, Arculus R, Lilley M, Butterfield D, Resing J, Baker E, Embley R (2015) Helium isotope, C/3He, and Ba-Nb-Ti signatures in the northern Lau Basin: Distinguishing arc, back-arc, and hotspot affinities. Geochem Geophys Geosyst 16(4):1133-1155. doi: 1110.1002/2013GL057681
- Michael PJ, Escrig S, Rubin KH, Cooper LB, Langmuir CH, Clague DA, Keller Ns, Plank T (2009) Major and Trace Elements and Volatiles in Glasses from the 2009 Rapid Response Expedition to West Mata Volcano and Northeast Lau Spreading Center (NELSC). Abstract V51D-1720 presented at 2009 Fall Meeting of American Geophysical Union, San Francisco, CA
- Millen DW, Hamburger MW (1998) Seismological evidence for tearing of the Pacific plate at the northern termination of the Tonga subduction zone. Geology 26(7):659-662
- Park J-W, Campbell IH, Kim J, Moon J-W (2015) The role of late sulfide saturation in the formation of a Cu-and Au-rich magma: Insights from the platinum group element geochemistry of Niuatahi–Motutahi lavas, Tonga rear arc. J Petrol 56(1):59-81. doi: 10.1093/petrology/egu1071
- Pelletier B, Calmant S, Pillet R (1998) Current tectonics of the Tonga–New Hebrides region. Earth Planet Sci Lett 164(1):263-276
- Perfit MR, Chadwick WW (1998) Magmatism at mid-ocean ridges: Constraints from
 volcanological and geochemical investigations. In: W. R. Buck PTD, J. A. Karson, Y.
 Lagabrielle (ed) Faulting and Magmatism at Mid-Ocean Ridges. Geophysical Monograph
 106, American Geophysical Union, Washington, D.C., pp 59-116.
- Resing JA, Lilley MD, Lupton JE, Embley RW, Buck N, Walker SL, Olson EJ, Dziak RP,
 Baumberger T (2010) Hydrothermal Activity and its Chemical Characteristics in the NE
 Lau Basin. Abstract T13B-2187, presented at 2010 Fall Meeting, AGU, San Francisco,
 Calif

Resing JA, Rubin KH, Embley RW, Lupton JE, Baker ET, Dziak RP, Baumberger T, Lilley M, Huber J, Shank T, Butterfield DA, Clague D, Keller N, Merle S, Buck N, Michael P, Soule A, Caress D, Walker S, Davis R, Cowen J, Reysenbach A-L, Thomas H (2011)
Active submarine eruption of boninite in the northeastern Lau Basin. Naure Geoscience 4:799-806. doi:710.1038/NGEO1275

- Rubin KH, Embley RW (2012) Identification and implications of a submarine monogenetic field in the NE Lau Basin. Abstract V44C-08 presented at 2012 Fall Meeting, AGU, San Francisco, Calif, 3-7 Dec
- Rubin KH, Embley RW, Arculus RJ, Lupton JE (2013) Magmatically Greedy Reararc Volcanoes of the N. Tofua Segment of the Tonga Arc. Abstract V13I-04 presented at 2013 Fall Meeting, AGU, San Francisco, Calif, 9-13 Dec
- Rubin KH, Michael P, Jenner F, Clague DA, Glancy S, Hellebrand E, Arculus R, Gill J, Todd E, E. LJ, Embley RW (2015) Composition within and between Tonga arc/Lau Basin backarc eruptions reveal wide variety of parent melts linked to eruption styles. Goldschmidt Conference Abstracts, 2015, Prague, Czech Republic, 08/2015:https://goldschmidt.info/2015/uploads/abstracts/finalPDFs/A-Z.pdf
 - Saunders AD, Tarney J (1979) The geochemistry of basalts from a back-arc spreading centre in the East Scotia Sea. Geochim Cosmochim Acta 43(4):555-572
 - Schmitt AK, Perfit MR, Rubin KH, Stockli DF, Smith MC, Cotsonika LA, Zellmer GF, Ridley WI, Lovera OM (2011) Rapid cooling rates at an active mid-ocean ridge from zircon thermochronology. Earth Planet Sci Lett 302:349-358. doi.org/10.1016/j.epsl.2010.12.022
 - Sigurdsson H, Sparks RSJ (1981) Petrology of rhyolitic and mixed magma ejecta from the 1875 eruption of Askja, Iceland. J Petrol 22(1):41-84.
 - Sinton J, Bergmanis E, Rubin K, Batiza R, Gregg TK, Grönvold K, Macdonald KC, White SM (2002) Volcanic eruptions on mid-ocean ridges: New evidence from the superfast spreading East Pacific Rise, 17–19 S. Journal of Geophysical Research: Solid Earth 107(B6):ECV 3-1-ECV 3-20. doi:10.1029/2000JB000090
 - Sinton JM, DS Wilson, DM Christie, DM Hey, RN, Delaney JR (1983) Petrological consequences of rift propagation on oceanic spreading ridges. Earth Planet Sci Lett 62:193-207
 - Smith DK, Cann JR (1993) Building the crust at the Mid-Atlantic Ridge. Nat Resour 365(6448):709-714
 - Spera FJ (2000) Physical Properties of Magmas. In: Sigurdsson H, Houghton B, McNutt S, Rymer H, Stix J (eds) Encyclopedia of volcanoes. Elsevier, pp 171-190
 - Stakes DS, Perfit MR, Tivey MA, Caress DW, Ramirez T, Maher N (2006) The Cleft revealed: Geologic, magnetic, and morphologic evidence for construction of upper oceanic crust along the southern Juan de Fuca Ridge. Geochem Geophys Geosyst 7(4). doi:10.1029/2005GC001038.
 - Stern RJ, Tamura Y, Embley RW, Ishizuka O, Merle SG, Basu NK, Kawabata H, Bloomer SH (2008) Evolution of West Rota Volcano, an extinct submarine volcano in the southern Mariana Arc: Evidence from sea floor morphology, remotely operated vehicle observations and ⁴⁰Ar–³⁹Ar geochronological studies. Island Arc 17(1):70-89
- Stern RJ, Tamura Y, Ishizuka O, Shukano H, Bloomer SH, Embley RW, Leybourne M,
 Kawabata H, Nunokawa A, Nichols AR (2014) Volcanoes of the Diamante cross-chain:

913 evidence for a mid-crustal felsic magma body beneath the Southern Izu-Bonin-Mariana 914 arc. Geological Society, London Special Publications 385(1):235-255 915 Takeuchi S (2011) Preeruptive magma viscosity: An important measure of magma eruptibility. 916 Journal of Geophysical Research: Solid Earth 116(B10). doi:10.1029/2011JB008243 917 Takeuchi S (2015) A melt viscosity scale for preeruptive magmas. Bull Volcanol 77. 918 doi:10.1007/s00445-00015-00929-00448 919 Taylor B, Martinez F (2003) Back-arc basin basalt systematics. Earth Planet Sci Lett 210(3):481-920 497. doi:410.1016/0012-1821X(1096)00148-00143 921 Taylor R, Nesbitt RW, Vidal P, Harmon RS, Auvray B, Croudace IW (1994) Mineralogy, 922 chemistry, and genesis of the boninite series volcanics, Chichijima, Bonin Islands, Japan. 923 J Petrol 35(3):577-617 924 van Keken PE, Hacker BR, Syracuse EM, Abers GA (2011) Subduction factory: 4. Depth -925 dependent flux of H2O from subducting slabs worldwide. Journal of Geophysical 926 Research: Solid Earth 116(B1). doi:01410.01029/02010JB007922 927 Walker GP (1991) Structure, and origin by injection of lava under surface crust, of tumuli, "lava 928 rises", "lava-rise pits", and "lava-inflation clefts" in Hawaii. Bull Volcanol 53(7):546-558 929 Wanless VD, Perfit MR, Ridley WI, Klein E (2010) Dacite petrogenesis on mid-ocean ridges: 930 evidence for oceanic crustal melting and assimilation. J Petrol 51 (12):2377-2410. 931 doi:2310.1093/petrology/egq2056 932 White SM, Macdonald KC, Haymon RM (2000) Basaltic lava domes, lava lakes, and volcanic 933 segmentation on the southern East Pacific Rise. Journal of Geophysical Research: Solid 934 Earth 105(B10):23519-23536. doi:10.1029/2000JB900248 935 Whittington AG, Hellwig BM, Behrens H, Joachim B, Stechern A, Vetere F (2009) The 936 viscosity of hydrous dacitic liquids: implications for the rheology of evolving silicic 937 magmas. Bull Volcanol 71(2):185-199. doi:10.1007/s00445-008-0217-y 938 Wiens DA, Kelley KA, Plank T (2006) Mantle temperature variations beneath back-arc 939 spreading centers inferred from seismology, petrology, and bathymetry. Earth Planet Sci 940 Lett 248(11):30-42. doi:10.1016/j.epsl.2006.1004.1011 941 Wilson L, Parfitt EA (1993) The formation of perched lava ponds on basaltic volcanoes: the 942 influence of flow geometry on cooling-limited lava flow lengths. J Volcanol Geotherm 943 Res 56(1):113-123 944 Wright IC, Gamble J (1999) Southern Kermadec submarine caldera arc volcanoes (SW Pacific): 945 caldera formation by effusive and pyroclastic eruption. Mar Geol 161(2):207-227 946 Wright IC, Worthington TJ, Gamble JA (2006) New multibeam mapping and geochemistry of 947 the 30°-35° S sector, and overview, of southern Kermadec arc volcanism. Journal 948 Volcanol Geotherm Research 149:263-296. doi:10.1016/j.jvolgeores.2005.03.021 949 Zellmer KE, Taylor B (2001) A three-plate kinematic model for Lau Basin opening. 950 GeochemGeophys Geosyst 2(5):doi:10.1029/2000GC000106 951

952

Figure Captions

954

975

contour values.

955 Fig. 1: Map of NE Lau basin (location: see inset map) with major features labeled as: MTJSC-956 Mangatolu Triple Junction spreading center; FRSC – Fonualei Rift spreading center; 957 NELSC – Northeast Lau spreading center. Dashed blue line is approximate trace of 958 center of neovolcanic zones on spreading centers; dashed red line is approximate trace of 959 topographic low of Tonga Trench. Brown line is 1000 m contour of northern Tofua Arc. 960 Gray arrow labeled 157 mm/yr is vector for relative motion between Tonga and 961 Australian plates (Zellmer and Taylor 2001). Gray lines are 1000 m contours. Box 962 encloses area shown in Figures 2-4. 963 Fig. 2: Niuatahi lava corridor multibeam bathymetry with dacite lava flow fields highlighted in 964 grayish overtones bounded by red lines. Boundaries outline areas of higher backscatter 965 and small-scale topography indicative of lava flow morphology such as pits, channels, 966 flow fronts, and lobes. Green dashed line bounding light brown overtone across SE 967 portion of map shows approximate limit of volcaniclastic apron of Tofua Arc. Black 968 dashed line is axis of Northeast Lau spreading center (NELSC). Lava flow fields are 969 named in black letters LL-A (1-5), LL-B, LL-B1, LL-C, and LL-D designate Lau lava 970 flow fields named in text. White patches within lava flow boundaries are kipukas 971 (patches of older seafloor). Niuatahi (N), Motutahi (Mo), West Mata (WM), and BoCo are 972 seamounts or volcanic cones referred to in text. NR is older ridge extending north from 973 Niuatahi, and MB is Mata Basin, a rifted region containing the Mata seamounts. Grid cell 974 size of bathymetry grid is 20 m. Gray lines are 250 m contours with italicized numbers as Fig. 3: Niuatahi lava corridor acoustic backscatter from multibeam surveys (see color table in legend for relative values with minus values highest acoustic return). Letter and line designations are same as Fig. 2.

976

977

978

994

995

996

997

998

- 979 Fig. 4: Niuatahi lava corridor features with sample and camera tow locations. Numbers in white 980 filled boxes (cruise KM1024) and circles (cruise KM1129a) are dredge numbers (Table 1 981 and ESM 1) for samples used in this study. Thick black lines (not numbered) are dredges 982 (length defined by begin and end time of dredges on bottom) recovering boninitic 983 composition on cruises KM1024 and KM1129a (unpublished data). Numbered thick 984 yellow and red lines are, respectively, dredges recovering dacite and (one) rhyolite 985 samples. Black filled, yellow filled and red filled triangles are, respectively, boninite 986 dacite and rhyolite dredge samples reported in Falloon et al. (2007). Brown-filled triangle 987 near top left of map is location of back-arc basin basalt dredge sample reported by 988 Falloon et al. (2007). Filled black square on summit of West Mata (WM) is location of 989 boninite sample reported in Resing et al. (2011). Thin black lines adjacent or overlapping 990 with dredges 04, 06 and 07 are paths across bottom of camera tows shown in detail in 991 Fig. 10. Rectangular outlines show location of Figures 8 (LL-A3), 9c (LL-B), 10c (LL-992 C), and 13 (LL-D). Note that lava flow fields outlined in red also mark higher backscatter 993 zones (see Figure 3).
 - Fig. 5: 3D oblique perspective images created using Fledermaus© supported by QPS Marine and Hydrographic Solutions. White lines show outlines of dacite lava flow fields: (a)

 View of Lau lavas looking southwest toward Niuatahi seamount; (b) LL-B flow field looking southwest;(c) Zoomed in view of LL-B flow field; LD is Lava Depression; (d)

 LL-D flow field looking to southeast.

999 Fig. 6: Photos of dredge samples from NE Lau dredges: (a) Sample KM1024-D24-R04 from 1000 lava flow field LL-D showing glassy texture; (b) Sample KM1024-D04-R08 from lava 1001 flow field LL-C showing folded glassy layers; (c) Sample KM1024-D08-R02 showing 1002 "buffalo head hair" texture common on the dacite flow tops. Black scale bars are 25 cm. 1003 Fig. 7: Major element lava chemistry summary. The general color scheme used is: (1) warm 1004 colored triangles for large lava flow fields (LL-B, LL-C, and LL-D); (2) cold colored 1005 triangles for samples from Niuatahi caldera, rim, and LL-A lava fields. a) TAS plot of 1006 NE Lau lavas, dashed line is the current IUGS definition for the dacite-rhyolite divide; 1007 (b) detailed Harker plot Al₂O₃ vs. SiO₂ for LL-A-D fields; (c) detailed Harker plot of 1008 MgO vs. SiO₂ for LL-A-D fields; (d) detailed Harker plot of FeO vs. SiO₂ for LL-A-D 1009 fields; (e) TiO₂ versus MgO; (f) CaO/Al₂O₃ versus MgO. 1010 Fig. 8: Bathymetry of lava flow field LL-A3 (see Figure 4 for location box). Contours (gray 1011 lines) are at 100 m interval. Line A-B locates bathymetry cross-section profile (lower left 1012 inset). Southeast corner of map is northwest flank of Niuatahi. Dredges KM-1024-D03 1013 and KM1129a-D15 noted. Lava extent as mapped by backscatter is the red outline and 1014 kipukas (older terrain surrounded by lava flow) are brown lines. Dashed lines with arrows 1015 indicate possible lava flow directions. 1016 Fig. 9: Details of lava flow field LL-B. Bathymetric dome-like hills discussed in text are labeled 1017 "D", lava depression labeled "LD", and lava channel labeled "LC". Backscatter boundary 1018 is thick black line and kipukas within the lava flow are outlined in blue. Small yellow 1019 patch southwest of West Mata is 2010 eruption as described in Embley et al. (2014). a) 1020 Multibeam bathymetry of LL-B lava flow field at 20 m grid-cell size. b) Bathymetric 1021 slope of same area as (a) color coded with slope range in degrees as in color bars. (c)

1022

1023

1024

1025

1026

1027

1028

1029

1030

1031

1032

1033

1034

1035

1036

1037

1038

1039

1040

1041

1042

1043

Features of LL-B lava flow field. Orange-shaded areas are possible lava domes on ridge next to lava flows. Lava flow levels marked in italic Roman numerals (*I-IV*) as in inset. Irregular brown lines within LL-B are possible flow fronts. Square boxes with numbers next to thick yellow lines are dredges and circular symbols with numbers next to black lines are camera tows. Arrows represent possible flow directions. Inset shows bathymetric profile (along dashed line A-B on map) showing different levels of lava surface (I-IV).

Fig. 10: Detailed maps of camera tow sites on LL-B and LL-C. On-bottom camera tow tracks are black lines. Thick yellow lines are on-bottom dredge tracks (labeled). Contour interval is 10 m on all maps and thick red line is boundary of high acoustic backscatter zones (except for "a", which lies completely within high backscatter zone of LL-B). Insets on upper left of each panel is along-track depth profile constructed by adding pressure depth from the camera CTD and the height above bottom from the altimeter mounted on the camera. Small arrows and lower case letters show locations of camera images shown in Figure 11. (a) Close-up map of lava depression (LD) within LL-B lava flow field with track of camera tow CT-01. Location of map on Figure 9c (box over feature labeled "LD"), (b) Close-up map of shallow portion of northwest portion of LL-B lava flow field with track of camera tow CT-02. Location in Figure 9c (box just below inset). Profile on inset starts just east of the backscatter boundary (red line on map), position marked by arrow going from left side of inset. (c) Map of southwest portion of LL-C lava flow field camera tow CT-05 across lava flows within LL-C field. "SF and "NF" are, respectively, north mound and flows. Location on Fig. 4.

1044

1045

1046

1047

1048

1049

1050

1051

1052

1053

1054

1055

1056

1057

1058

1059

1060

1061

1062

1063

1064

1065

Fig. 11: Lava flow gray scale images from camera tows CT-01, CT-02, and CT-05. Locations are noted on insets in Figure 10. All photos were auto-processed in ©Adobe Photoshop Elements to obtain relatively uniform contrast. Approximate long-axis of frames vary between approximately 4 and 9 m. (a) CT-01 photo looking down into depression west of lava depression on LL-B; (b) CT-01 image of broken ropey sheet flow west of lava depression; (c) intact surface of ropey flow (large fold in middle of frame ~ 1.5-2.0 m across) on floor of lava depression, CT-01; (d) pillow tubes on slope (~ 1 m diameter tubes), CT-02; (e) pillows (≥ 1 m diameter each) amidst blocky flows, CT-02; (f) spinose extrusion site ~5 m across, CT-02; (g) Lines of extrusion produced along expanding fractures, CT-02; (h) extensional cracks in lava flow, CT-02; (i) ropey surface (frame ~6 m on long axis), CT-02; (j) ropey surface along CT-02; (k) endogenous ridge with large axial fracture (frame ~8 m across), CT-02; (1) similar to Fig. 11k with possible crease structures as discussed in text (frame ~8 m across), CT-02; (m) anastomosing pillow tubes up to ~2m diameter, CT-05; (n) extrusion at end of pillow tube (~3-4 m across) along tri-crack, CT-05; (o) Pillows, CT-05. Note surface which resembles "buffalo head hair" texture shown on Figure 6c; (p) Looking down into longitudinal fracture of endogenous ridge with columnar jointed lavas, CT-05.

Fig. 12: Mosaics of NE Lau dacite lavas created by overlapping and rescaling photos from Camera Tows CT-02. Scale of each approximately 20-25 m on long axis: (a) overlap of pillow tube lavas edge of lava dome; (b) Anastomosing pillow tubes on slope, CT-05.

Fig. 13: Bathymetry of lava flow filed LL-D. Red line is backscatter boundary; dashed line is path of bathymetric cross section shown below. Roman numerals I-V represent levels of

lava surface, letters A-E are keyed to changes in direction of cross-section, and letters a-c with arrows point to specific features discussed in text.

Electronic Supplement Captions:

ESM 1: Table of named locations, persistence identifiers, and location metadata

ESM_2: Accepted and measured values for STG-56 and VG-2 analyzed for unknowns

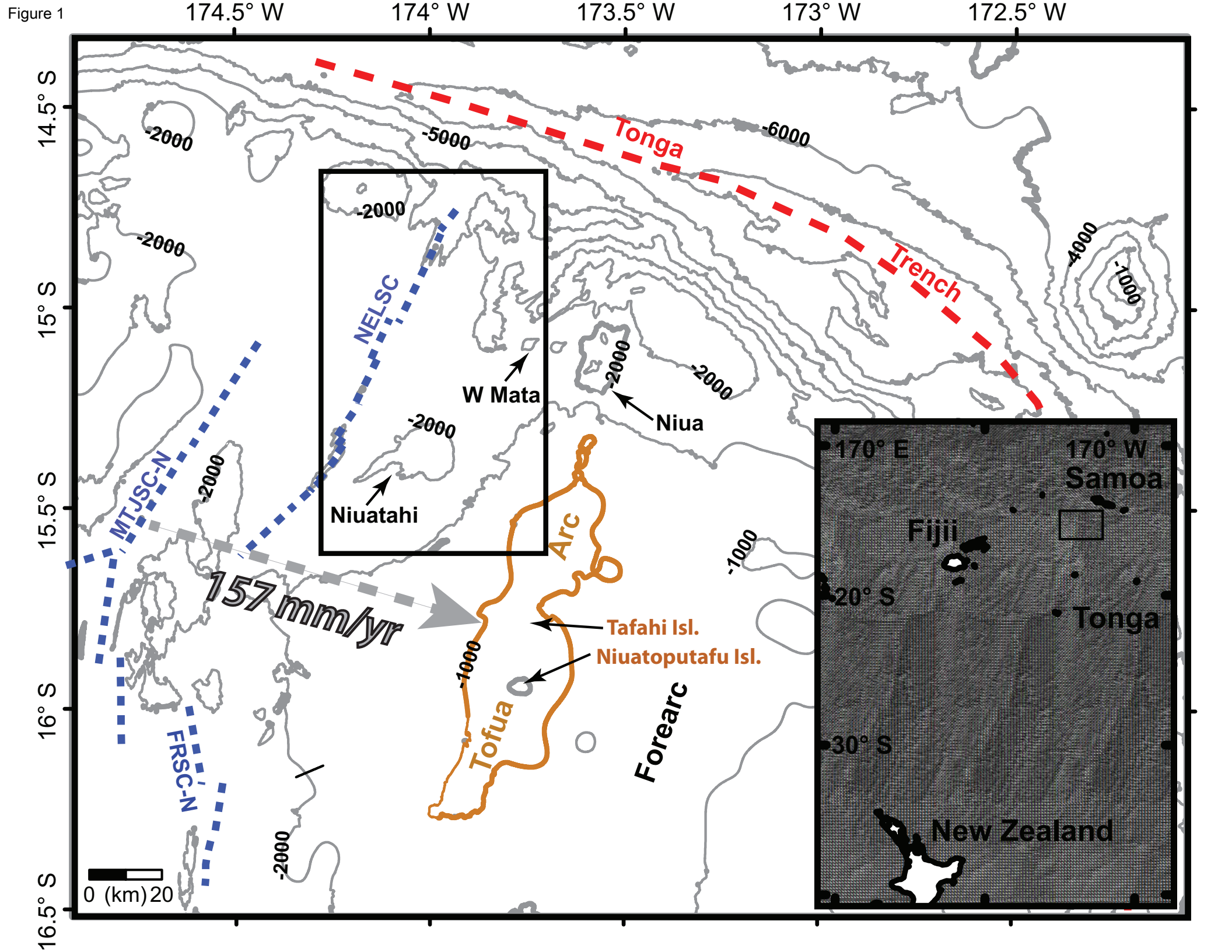
ESM_3: Six backscatter electron (BSE) images illustrating the range of groundmass textures in these submarine dacite lavas. A 100 μm scale bar is present in the lower right corner of each panel. The images are arranged in order of increasing degree of microcrystallinity. These groundmass textures develop primarily during lava emplacement, although some of the larger microphenocrysts (defined as < 100 μm in largest dimension) seen in all images likely grew in the magma just before eruption. White crystals are pyroxenes, dark grey are plagioclase, and the bulk of the grey material in each image is glass. Images were collected in backscatter electron mode on the University of Hawaii microprobe.

ESM_4: Lava compositions reported elsewhere in this paper plotted with three synthetic Liquid Lines of Descent (LLD) estimated using the MELTS program (adiabat_1ph_2-0) to investigate parent melt variations and differentiation effects. MELTS is not well calibrated for the conditions and magma compositions studied here, so these representative trends are used here only to demonstrate typical differentiation pathways and slopes. The LLDs are calculated starting from average West Mata boninite composition for three different conditions: The red colored LLD is for 500 bars pressure,

oxygen fugacity at QFM (quartz-fayalite-magnetite), and 2 weight % water; The green colored LLD is for 1000 bars pressure, oxygen fugacity at QFM +1, and 3 weight % water; The Blue colored LLD is for 1500 bars pressure, oxygen fugacity at QFM +1, and 4 weight % water. The trends demonstrate that a boninite parent melt can differentiate to make dacite magma with compositions similar to those observed in the large lava flow fields and at Niuatahi. However, a single boninite parent magma cannot make the full suite of compositions observed in the large lava flows and Niuatahi because some of the large lava flow compositional trends crosscut the LLD trends in some panels, suggesting mixing between magmas from different parents.

ESM_5: Movie made from still fames along track of CT-02 (using WHOI TowCam) showing dacite lava flow morphology within LL-B lava flow field. Camera towed \sim 5 m above bottom in 2500-2520 m water depth. Size of view between \sim 2-5 m across, varying with altitude. Transect \sim 200 m.

ESM_6: Movie made from still fames along track of CT-05 (using WHOI TowCam) showing dacite lava flow morphology within LL-C lava flow field. Camera towed ~5 m above bottom in 2500-2520 m water depth. Size of view between ~2-5 m across, varying with altitude. Transect ~200 m.



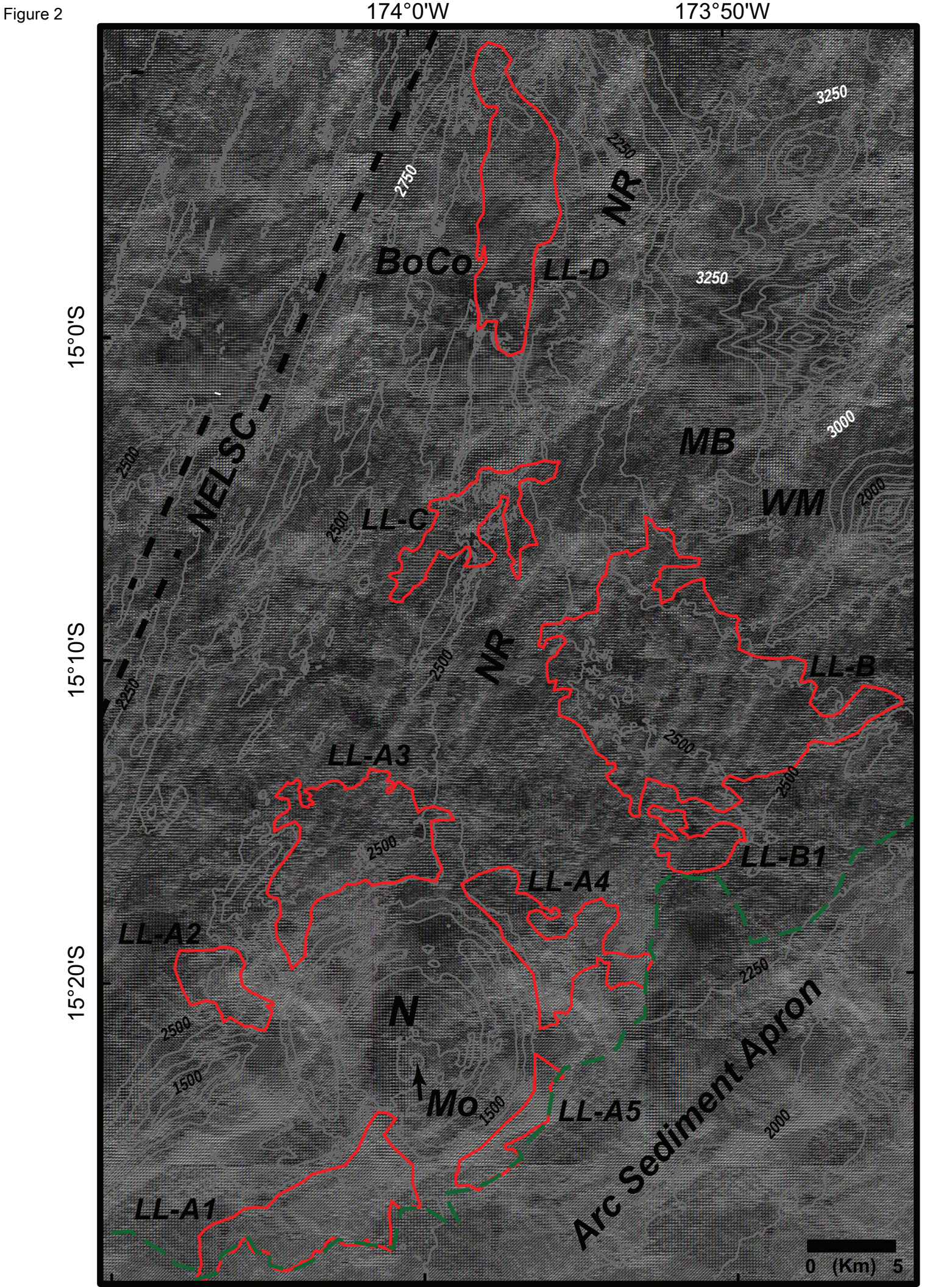
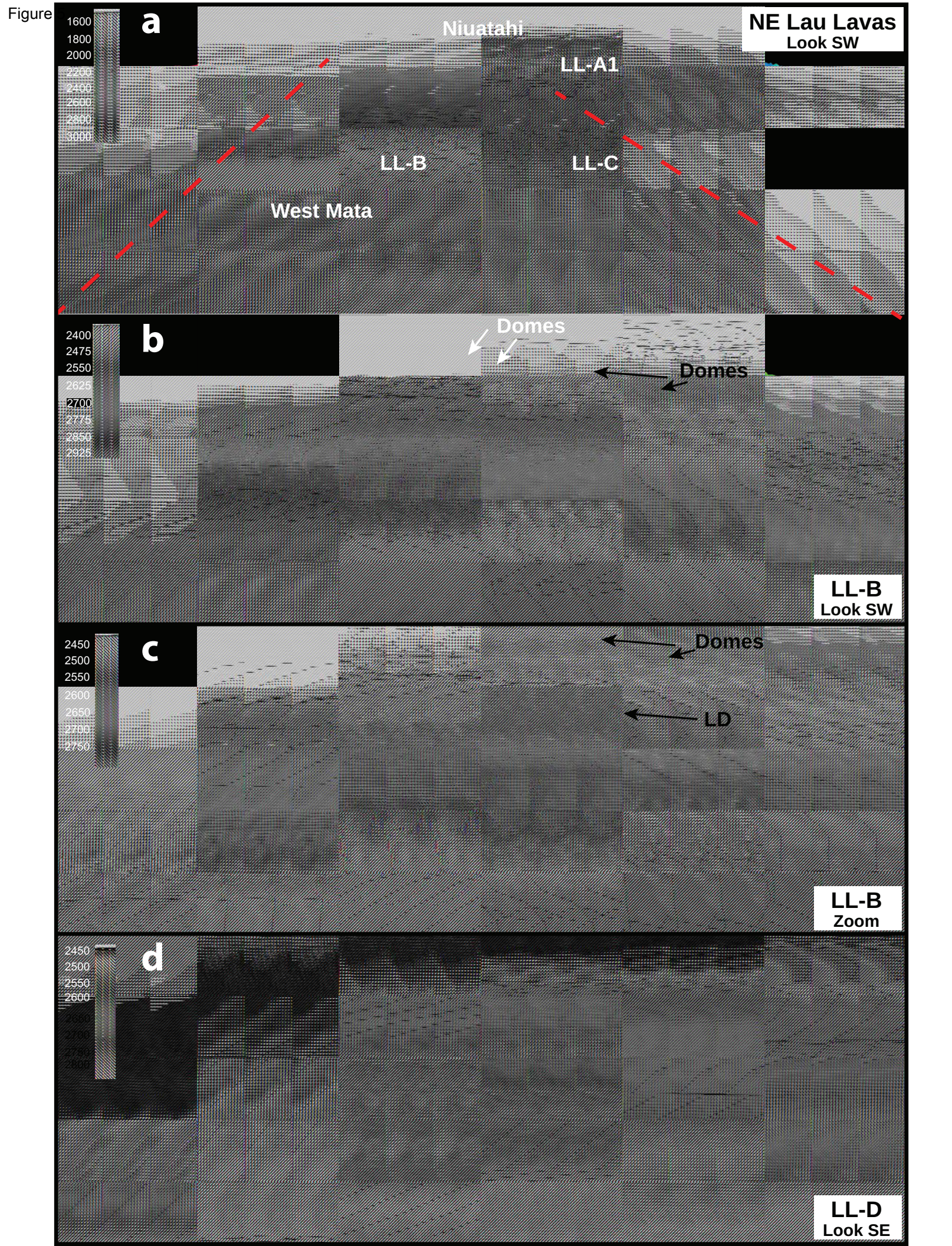
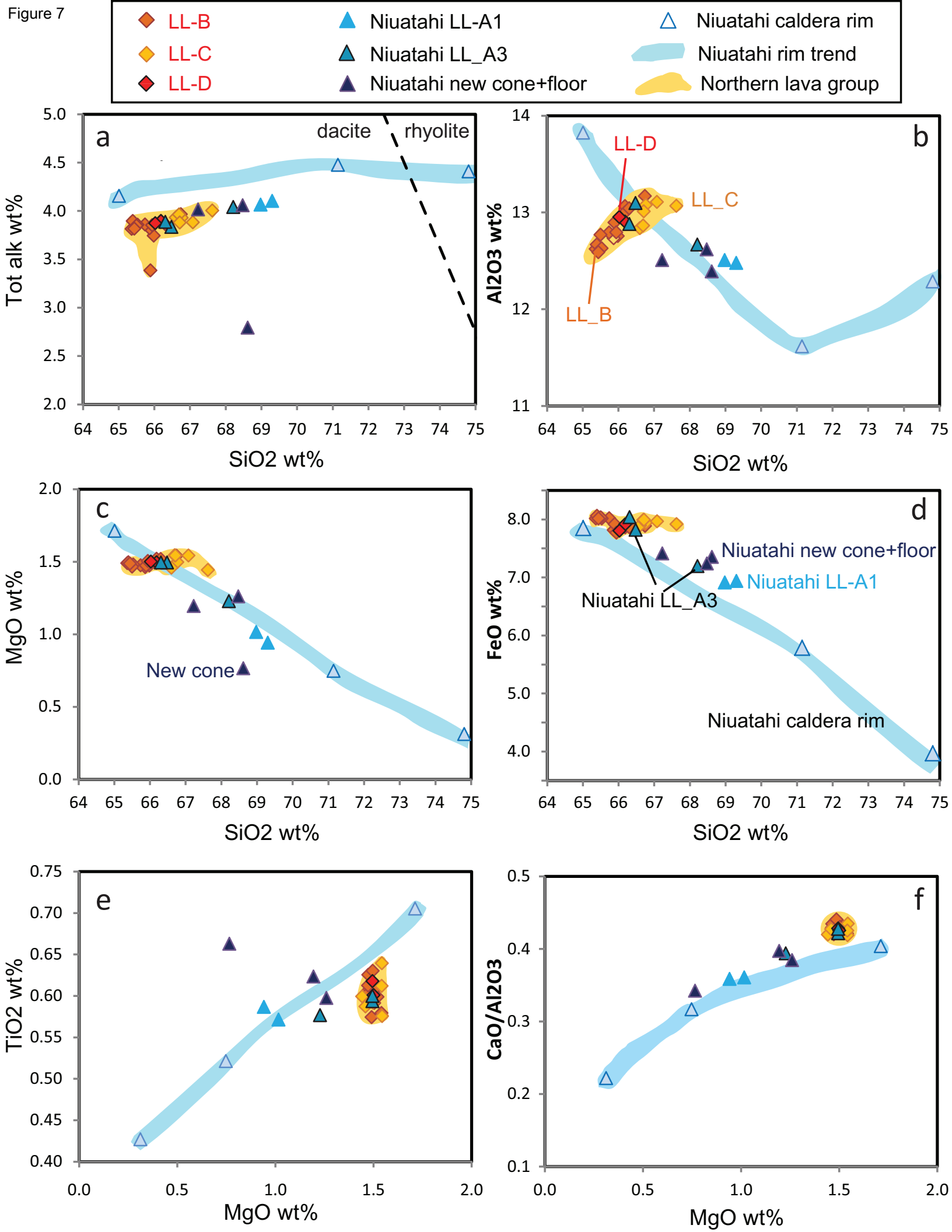


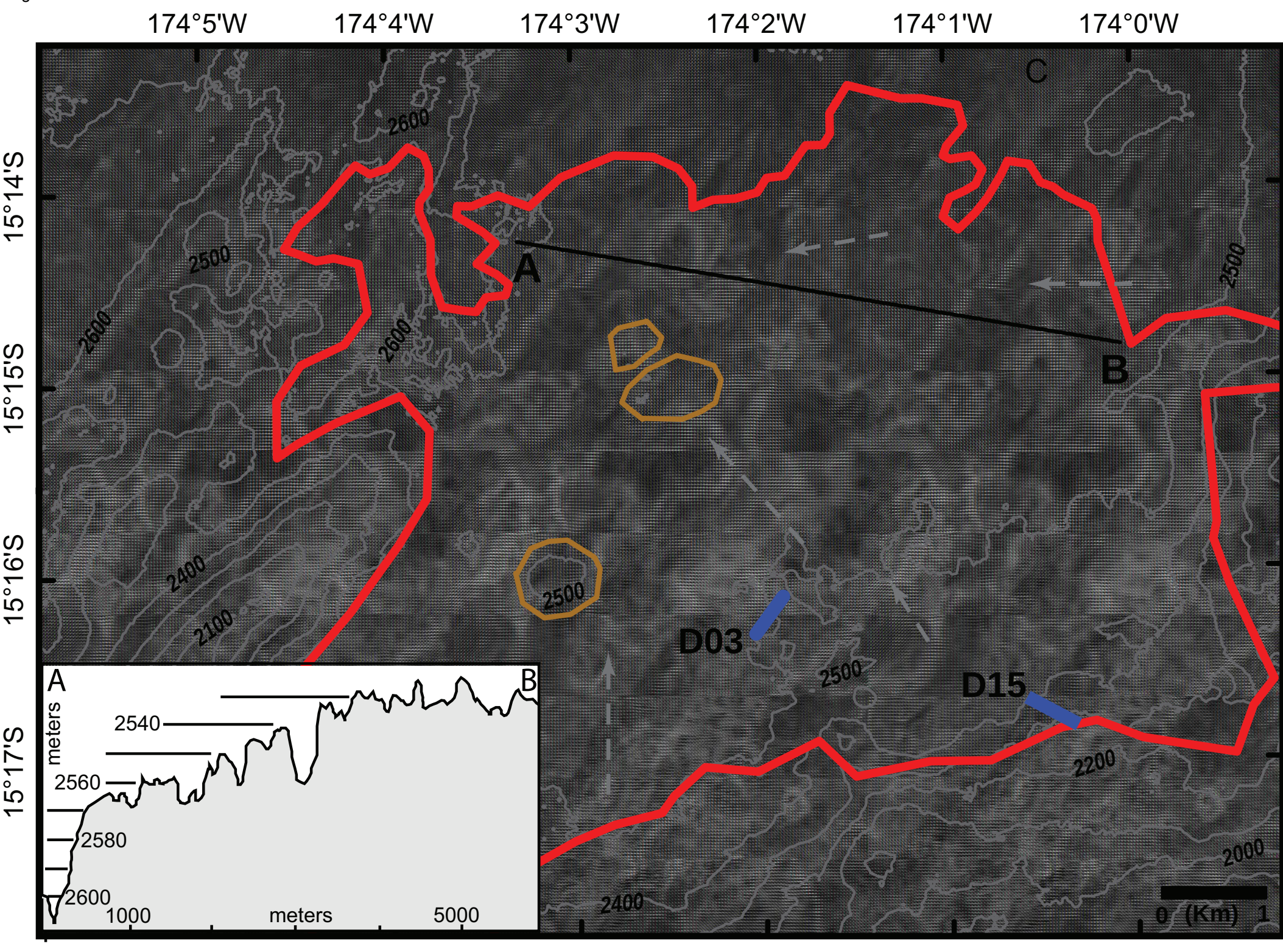
Figure 3

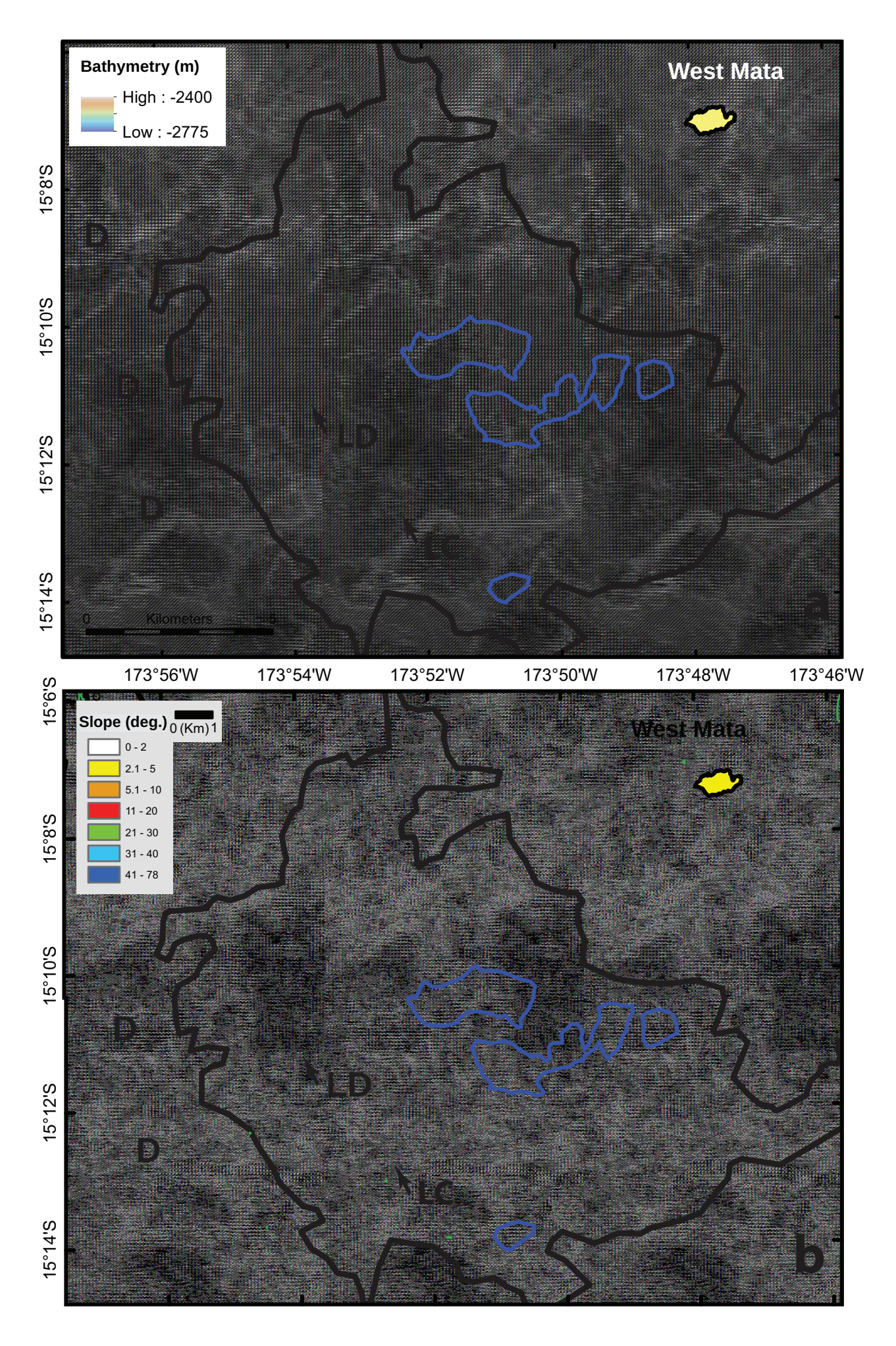


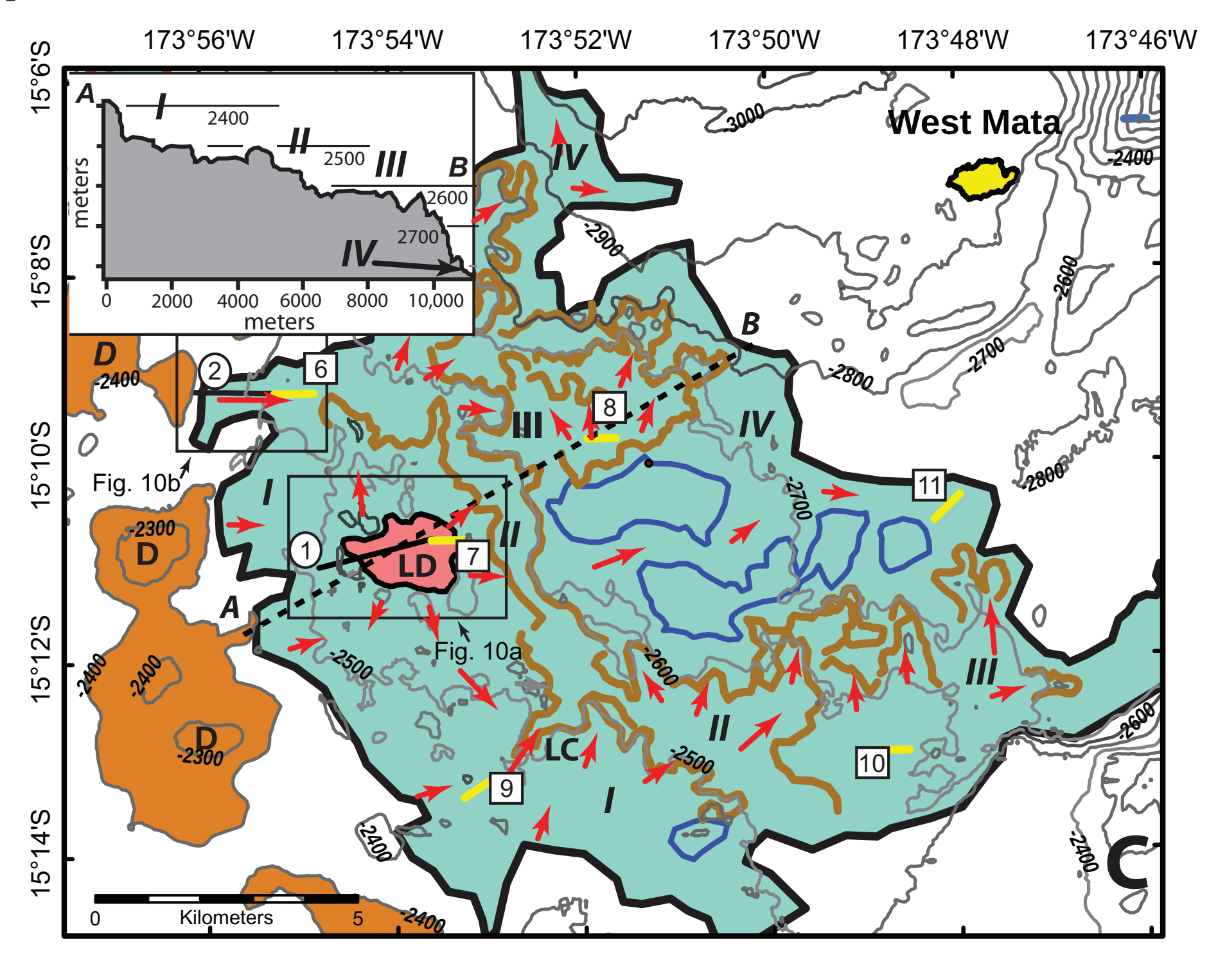
a KM1024-D24-R04 b KM1024-D04-R08 C

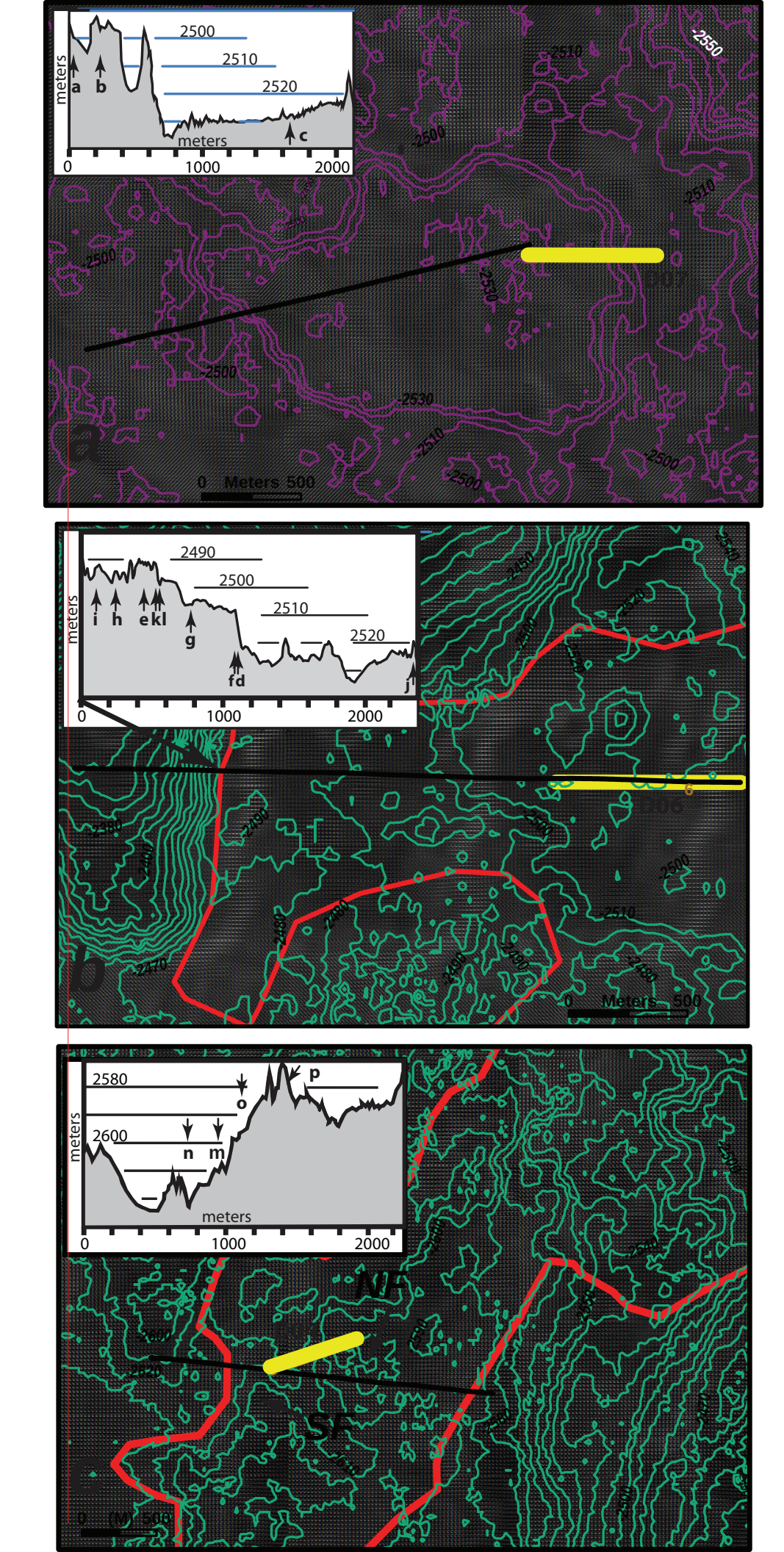
KM1024-D08-R02

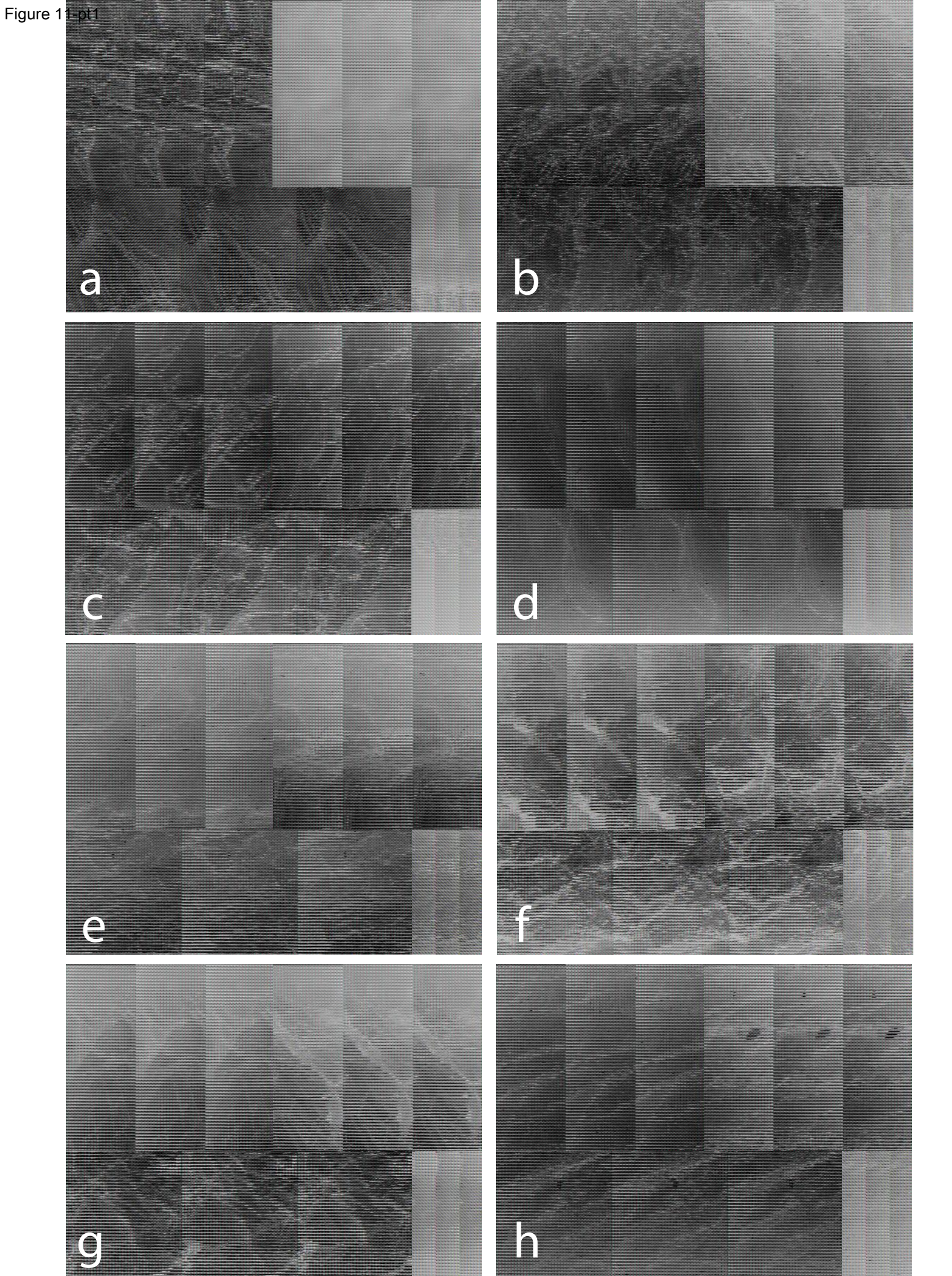


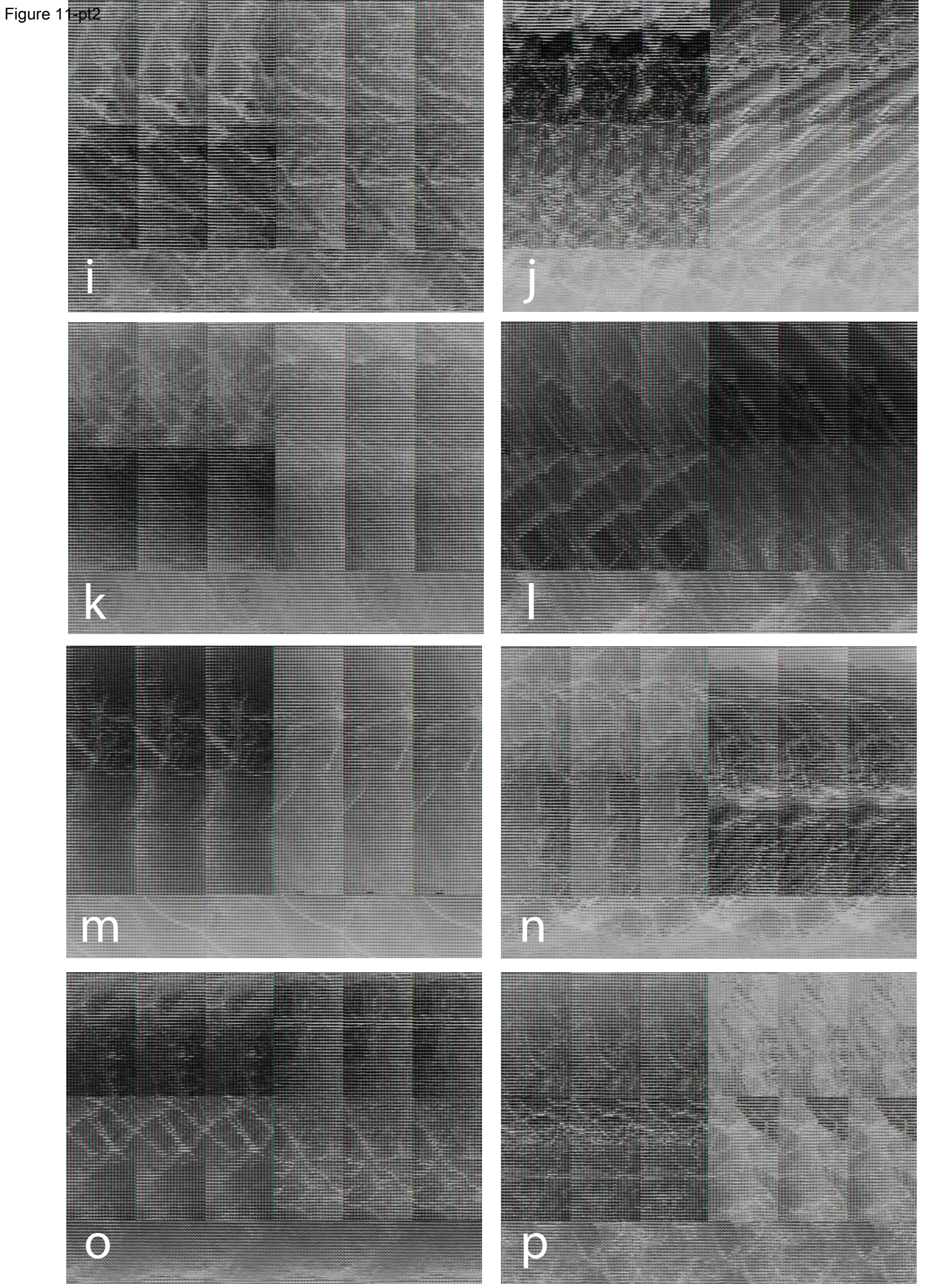


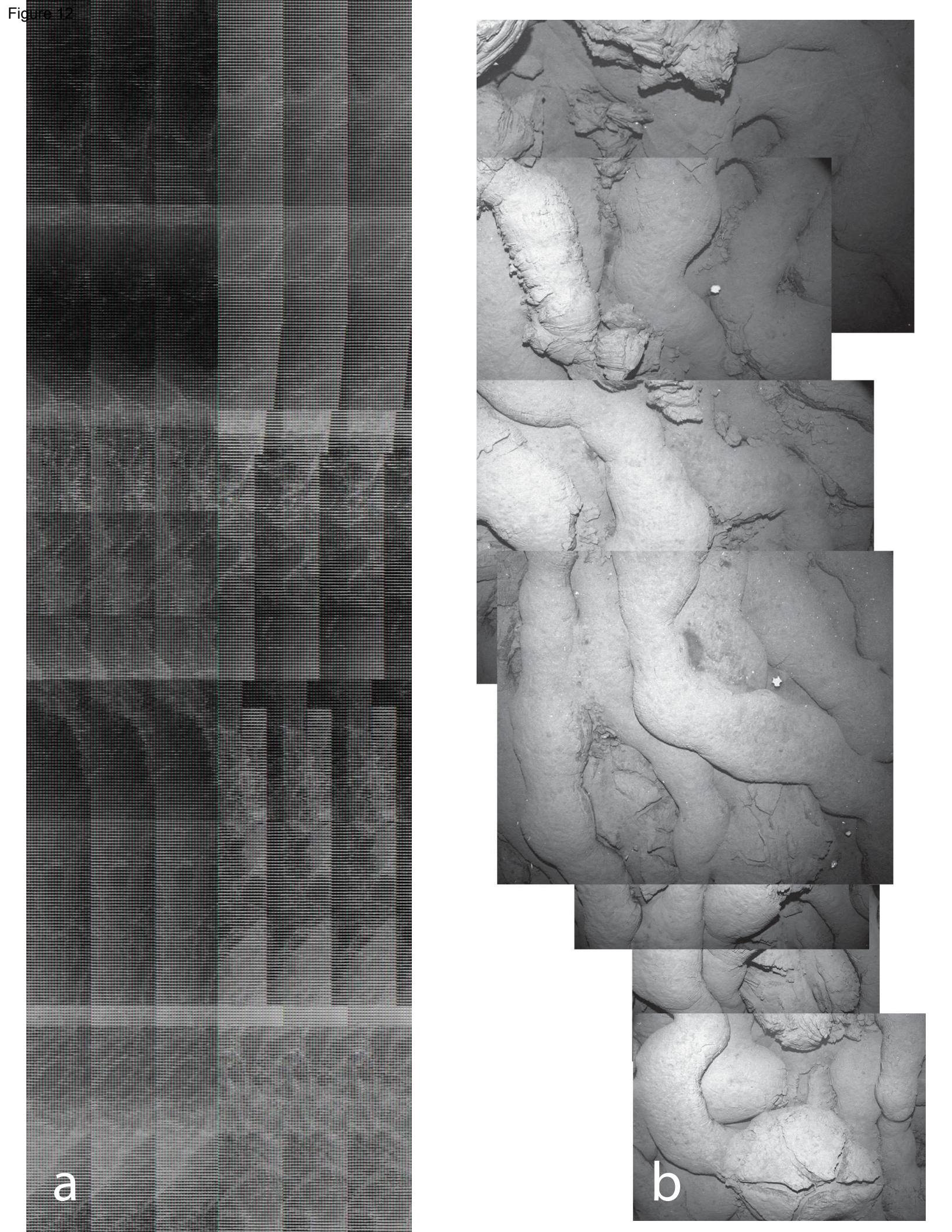












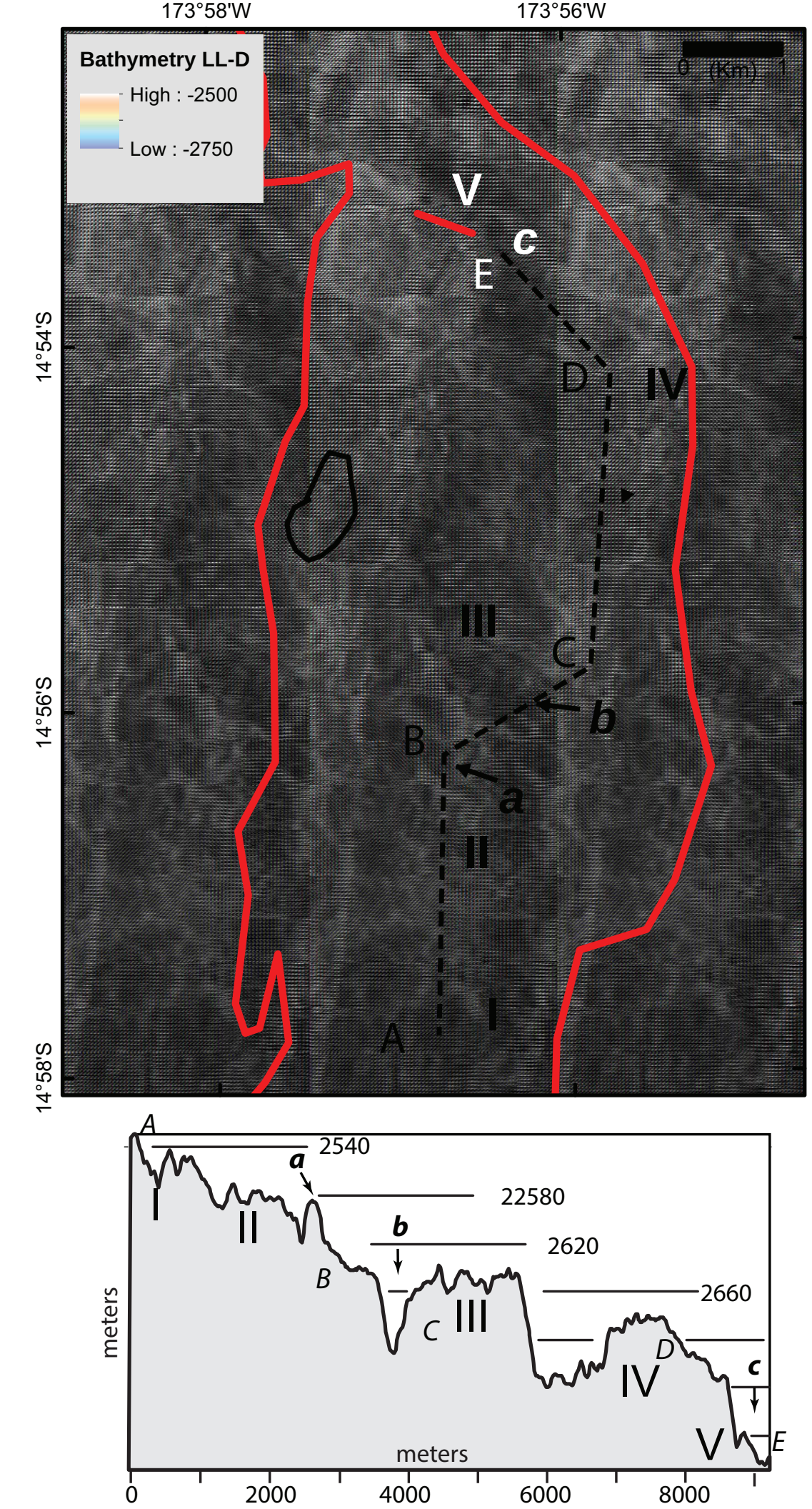


Table 1. Volcanic Glass Composition by Electron Microprobe

		-		SiO ₂	TiO ₂	Al ₂ O ₃	FeO	MnO	MgO	CaO	Na₂O	K ₂ O	P ₂ O ₅	Sum	Total	CaO
Locaton	Sample Name	Site Description	IGSN	wt %	wt %	wt %	wt %	wt %	wt %	wt %	wt %	wt %	wt %	%	Alk	Al_2O_3
Niuatahi	KM1008-CT08-1	Mohutahi Cone	KHR000026	68.62	0.66	12.39	7.35	0.12	0.77	4.24	1.66	1.13	0.22	97.60	2.79	0.34
	KM1008-CT08-2	Mohutahi Cone	KHR000027	67.23	0.62	12.51	7.41	0.13	1.19	4.97	2.92	1.10	0.22	98.68	4.02	0.40
	KM1129a D14-R02	NE caldera floor	KHR000186	68.47	0.60	12.62	7.24	0.14	1.26	4.85	3.01	1.05	0.20	99.88	4.06	0.38
	KM1129a D11-R01 †	SW flank	KHR000170	74.81	0.43	12.29	3.97	0.09	0.31	2.72	2.61	1.80	0.06	99.47	4.41	0.22
	KM1129a D26-R01	SE side	KHR000223	71.15	0.52	11.61	5.79	0.12	0.75	3.68	2.85	1.62	0.19	98.61	4.48	0.32
	KM1129a D12-R03 †	SW flank knoll	KHR00017a	65.01	0.71	13.82	7.85	0.15	1.71	5.58	2.84	1.32	0.19	99.53	4.16	0.40
Flows outside	KM1129a D13-R02	LL_A1	KHR000181	69.31	0.59	12.48	6.94	0.14	0.94	4.47	2.91	1.19	0.20	99.53	4.10	0.36
Niuatahi caldera	KM1129a D13-R03	LL_A1	KHR000182	68.98	0.57	12.51	6.91	0.14	1.02	4.51	2.87	1.19	0.18	99.23	4.06	0.36
	KM1024 D03-R01	LL_A3	KHR00002L	68.21	0.58	12.67	7.19	0.15	1.23	4.99	2.89	1.15	0.19	99.58	4.04	0.39
	KM1129a D15-R01	LL_A3	KHR000189	66.48	0.59	13.10	7.82	0.16	1.50	5.52	2.77	1.06	0.16	99.49	3.84	0.42
	KM1129a D15-R06	LL_A3	KHR00018e	66.31	0.60	12.88	8.04	0.16	1.50	5.51	2.81	1.08	0.20	99.41	3.89	0.43
Large lava flow fields	KM1024 D07-R01	LL_B	KHR00003A	65.99	0.63	12.76	7.83	0.16	1.47	5.52	2.67	1.08	0.18	98.58	3.74	0.43
	KM1024 D06-R06	LL_B	KHR000035	65.87	0.60	12.73	7.82	0.16	1.46	5.46	2.74	1.08	0.18	98.43	3.82	0.43
	KM1024 D06-R06	LL_B	KHR000035	65.37	0.57	12.62	8.02	0.15	1.49	5.54	2.74	1.07	0.20	98.11	3.81	0.44
	KM1024 D08-R02	LL_B	KHR00003N	65.74	0.61	12.79	8.02	0.16	1.47	5.55	2.79	1.07	0.19	98.70	3.86	0.43
	KM1024 D08-R08	LL_B	KHR00003T	65.39	0.63	12.67	8.06	0.15	1.50	5.54	2.83	1.06	0.19	98.35	3.90	0.44
	KM1024 D08-R10	LL_B	KHR00003V	65.53	0.60	12.63	8.02	0.15	1.48	5.54	2.80	1.06	0.19	98.33	3.86	0.44
	KM1024 D09-R03	LL_B	KHR000041	65.50	0.60	12.77	8.03	0.16	1.47	5.55	2.78	1.06	0.19	98.46	3.85	0.43
	KM1024 D09-R05	LL_B	KHR000043	65.44	0.61	12.59	8.02	0.15	1.49	5.54	2.76	1.05	0.20	98.19	3.82	0.44
	KM1024 D09-R06	LL_B	KHR000044	66.19	0.60	13.07	7.86	0.16	1.52	5.51	2.83	1.07	0.15	99.27	3.90	0.42
	KM1024 D10-R01	LL_B	KHR000046	66.18	0.61	13.00	7.89	0.15	1.49	5.52	2.83	1.06	0.18	99.24	3.89	0.42
	KM1024 D10-R03	LL_B	KHR000048	66.75	0.58	13.17	7.89	0.16	1.54	5.54	2.91	1.06	0.18	100.07	3.97	0.42
	KM1024 D10-R06	LL_B	KHR00004B	66.30	0.61	13.04	7.87	0.14	1.52	5.53	2.79	1.07	0.18	99.39	3.86	0.42
	KM1024 D11-R03	LL_B	KHR00004E	65.89	0.61	12.90	7.92	0.15	1.47	5.42	2.39	1.00	0.17	98.24	3.39	0.42
	KM1024 D11-R04	LL_B	KHR00004F	65.94	0.59	12.79	7.77	0.15	1.50	5.50	2.80	1.06	0.17	98.61	3.85	0.43
	KM1024 D04-R01	LL_C	KHR00002M	67.63	0.60	13.07	7.92	0.16	1.44	5.48	2.90	1.11	0.17	100.80	4.01	0.42
	KM1024 D04-R04	LL_C	KHR00002P	66.77	0.59	13.08	7.94	0.16	1.50	5.55	2.86	1.07	0.17	100.01	3.93	0.42
	KM1024 D04-R09	LL_C	KHR00002U	66.60	0.59	12.84	7.90	0.15	1.46	5.48	2.86	1.07	0.16	99.44	3.93	0.43
	KM1024 D05-R01	LL_C	KHR00002V	66.69	0.58	12.86	7.99	0.15	1.54	5.59	2.86	1.10	0.17	99.86	3.96	0.43
	KM1024 D05-R02	LL_C	KHR00002W	67.08	0.64	13.11	7.96	0.15	1.54	5.49	2.82	1.06	0.18	100.35	3.88	0.42
	KM1024 D05-R03	LL_C	KHR00002X	66.71	0.61	13.01	7.99	0.16	1.54	5.53	2.80	1.08	0.18	99.93	3.88	0.42
	KM1024 D24-R03	LL_D	KHR00006C	66.18	0.62	12.90	7.91	0.16	1.50	5.52	2.82	1.07	0.18	99.20	3.90	0.43
Neteri	KM1024 D24-R04	LL_D	KHR00006D	66.03	0.60	12.95	7.81	0.17	1.50	5.51	2.82	1.05	0.16	98.93	3.87	0.43

Notes:

Analyses were conducted using the University of Hawai'i JEOL JXA-8500F five-spectrometer electron microprobe (3 points per sample). All samples analyzed at 15 keV accelerating voltage, 10 nA beam current, and10 micron beam diameter, except two microcrystalline samples † (5 micron beam diameter). Count times (seconds) and spectrometer crystal were SiO₂ (50, TAP), TiO₂ (40, LIFH), Al₂O₃ (60, TAP) FeO (30, LIFH), MnO (40, LIFH), CaO (30, PETH), Na₂O (30, TAP), K₂O (40, PETJ), P₂O₅, (30, PETH). Three points on two different standards, VG-2 and STG-56 were measured as unknowns before and after every three samples (Supporting Information Table S2).

Table 2. NE Lau Dacite Lava Flow Statistics

Lava Flow	Area (km²)	No. Samples
Niuatahi Lava Fields		
LL-A1	49	1
LL-A2	15	0
LL-A3	55	2
LL-A4	34	0
<u>LL-A5</u>	<u>13</u>	<u>0</u>
Subtotal	166*	3
Northern Lava Fields		
LL-B	144	6
LL-B1	11	0
LL-C	26	2
<u>LL-D</u>	<u>55</u>	<u>1</u>
Subtotal	236	9
Total	402	12

^{*} Probably overestimate - some fields are likely mixtures of volcanic products